AD_____
(Leave blank)

Award Number:
W81XWH-08-1-0305

TITLE:
Specific PET Imaging Probes for Early Detection of Prostate Cancer Metastases

PRINCIPAL INVESTIGATOR:
Xiankai Sun

CONTRACTING ORGANIZATION:
University of Texas Southwestern Medical Center at Dallas
Dallas, Texas 75390

REPORT DATE:
May 2010

TYPE OF REPORT:
Annual

PREPARED FOR: U.S. Army Medical Research and Materiel Command
Fort Detrick, Maryland 21702-5012

DISTRIBUTION STATEMENT: (Check one)

Approved for public release; distribution unlimited

REPORT DOCUMENTATION PAGE

Form Approved
OMB No. 0704-0188

1. REPORT DATE *(DD-MM-YYYY)*	**2. REPORT TYPE**	**3. DATES COVERED** *(From - To)*
31/05/2010	Annual	1 MAY 2009-30 APR 2010

4. TITLE AND SUBTITLE
Specific PET Imaging Probes for Early Detection of Prostate Cancer Metastases

5a. CONTRACT NUMBER

5b. GRANT NUMBER
W81XWH-08-1-0305

5c. PROGRAM ELEMENT NUMBER

6. AUTHOR(S)

Xiankai Sun

xiankai.sun@utsouthwestern.edu

5d. PROJECT NUMBER

5e. TASK NUMBER

5f. WORK UNIT NUMBER

7. PERFORMING ORGANIZATION NAME(S) AND ADDRESS(ES)

*
University of Texas Southwestern Medical Center

Dallas, Texas 75390

8. PERFORMING ORGANIZATION REPORT NUMBER

9. SPONSORING / MONITORING AGENCY NAME(S) AND ADDRESS(ES)
U.S. Army Medical Research and Materiel Command
Fort Detrick, Maryland 21702-5012

10. SPONSOR/MONITOR'S ACRONYM(S)

11. SPONSOR/MONITOR'S REPORT NUMBER(S)

12. DISTRIBUTION / AVAILABILITY STATEMENT
Approved for public release; distribution unlimited

13. SUPPLEMENTARY NOTES
N/A

14. ABSTRACT: Polyarginines are a group of small peptides that have been used as drug delivery vehicles due to their capability of penetrating cell membranes. In one of our studies using such a peptide to deliver a therapeutic moiety to various prostate cancer cell lines, we surprisingly discovered that the peptide had remarkably high preference to prostate tissues. This specificity, which has not been reported before, prompted us to exploit this group of peptides for the early detection of prostate tumor metastases. Promisingly, in our preliminary studies, the peptide labeled with ^{64}Cu can clearly reveal metastases in a tumor-bearing animal model. By two-year work, we have successfully developed an approach to impart multivalency to a bifunctional chelator for targeted PET imaging probe design. This type of multivalent scaffolds features a chelator that forms a stable and neutral complex with a radiometal and multiple functional groups for multimeric presentation of targeting molecules. A bivalent scaffold was synthesized and coupled with an integrin $\alpha_v\beta_3$ targeting ligand, c(RGDyK), to afford a ^{64}Cu-labeled divalent probe. The in vitro and in vivo evaluation clearly demonstrated the divalent probe with the anticipated multivalent effect as compared to its monomeric counterpart. In addition, we have further demonstarted the imaging specificity of ^{64}Cu-DOTA-NHGR11 for prostate cancer detection.

15. SUBJECT TERMS - nONE PROVIDED.

16. SECURITY CLASSIFICATION OF:			**17. LIMITATION OF ABSTRACT**	**18. NUMBER OF PAGES**	**19a. NAME OF RESPONSIBLE PERSON**
a. REPORT	**b. ABSTRACT**	**c. THIS PAGE**			Xiankai Sun
unclassified	unclassified	unclassified	unlimited	28	**19b. TELEPHONE NUMBER** *(include area code)* 214-645-5978

Table of Contents

Introduction

The ultimate goal of this project is to develop specific PET imaging probes for early detection of distal metastases of prostate cancer. Based on one of our studies using a polyarginine (NH_2GR11) to deliver a therapeutic moiety to various prostate cancer cell lines, we hypothesize a new group of prostate-specific peptides could be developed as novel PET imaging probes using NH_2GR11 as lead compound for the detection of multi-foci extraprostatic spread of prostate cancer. Three specific aims are arranged to achieve the goals of this proposal: (I) Determine the mechanism of the prostate-specific uptake exhibited by NH_2GR11; (II) Design and synthesize novel BFC-peptide conjugates in order to achieve desired in vivo stability, pharmacokinetics, and enhanced prostate-specific binding affinity; and (III) Establish radiochemical protocols to label peptide conjugates with ^{64}Cu, and perform in vitro/*in vivo* evaluations of the potential prostate cancer-specific imaging agents.

Body

As shown in the first annual report, we completed the **tasks 1 – 5** in the first year of this project. In the 2nd year, our work was focused on the following tasks:

Task 5 (Months 6 – 12): Establishing radiochemical protocols to label the peptide conjugates with ^{64}Cu.

Radiolabeling of the peptide conjugates with ^{64}Cu is straightforward, the separation and purification will be carried out by either C-18 cartridge or HPLC.

Task 6 (Months 12 – 24): In Vitro Evaluation of the Radiolabeled Peptides.

The *in vitro* stability of the radiolabeled peptides or peptide conjugates will be determined by incubation at 37°C in fresh mammalian serum out to 24 h. Degradation of the radiolabeled compounds will be assessed at given time points (30-min, 1-h, 4-h, and 24-h) by the removal of an aliquot of sample for radio-TLC (C_{18} or silica gel solid phase) or radio-HPLC (C_{18} and size-exclusion column) analysis.

Task 7 (Months 12 – 32): In Vivo Evaluation of Radiolabeled Peptides.

Biodistribution experiments are planned with radiolabeled peptide conjugates. Urine excretion experiments will be carried out with the animal groups of the last time point of the biodistribution studies. Metabolic fate of the six ^{64}Cu-labeled compounds will be evaluated using 48 nude mice at two time points (1 h and 4 h; n = 4). The injection doses of biodistribution and metabolism studies are 5 – 10 μCi and 1 – 2 mCi, respectively, in a 100 – 150 μL volume diluted with saline. Pharmacokinetic parameters will be assessed by the procedures established in our preliminary studies with a two-compartment model using the same animals in the biodistribution experiments.

Research Progress in the 2nd year: We have successfully completed Tasks 5 – 7.

<u>Task 5: Establishing radiochemical protocols to label the peptide conjugates with ^{64}Cu</u>

HPLC condition: High performance liquid chromatography (HPLC) was performed on a Waters 600 Multisolvent Delivery System equipped with a Waters 2996 Photodiode Array a detector. The mobile phase was H_2O with 0.1% TFA (solvent A) and acetonitrile with 0.1% TFA (solvent B). The analytical analysis was performed on an XTerra RP18 Column with a gradient of 0% B to 100 % B in 50 min at a flow rate of 1.0 mL/min. The HPLC separation was performed on a semi-preparative XTerra RP18 Column with a gradient of 0% B to 100 % B in 50 min at a flow rate of 4.0 mL/min.

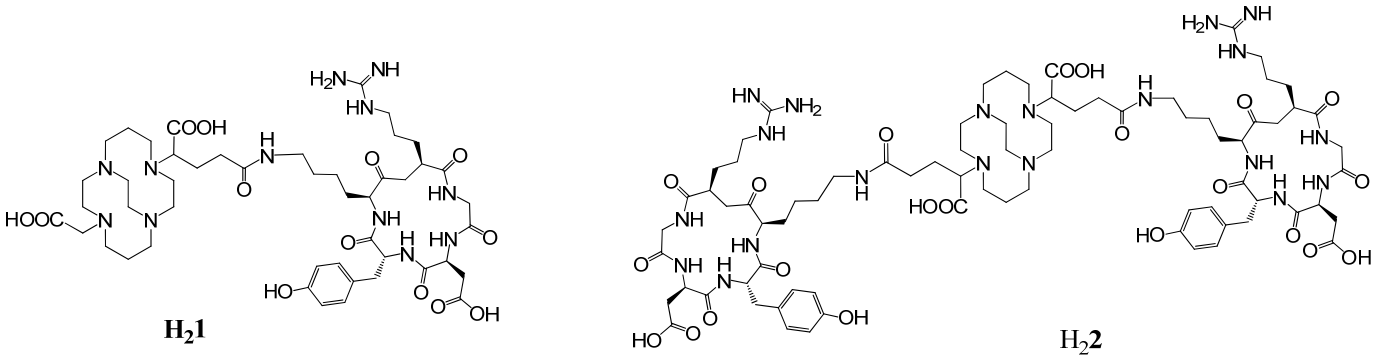

Scheme 1. Chemical structures of peptide conjugates H_2**1** and H_2**2**.

Radiolabeling of $H_2$1 or $H_2$2 with ^{64}Cu: To a 1.5 mL vial containing 5 μg of H_2**1** or H_2**2** in 200 μL of 0.4 M NH_4OAc (pH = 6.5) solution, 2 – 3 mCi of $^{64}CuCl_2$ in 0.1 M HCl was added. The reaction mixture was shaken and incubated at 75ºC for 0.5 h. Then, 5 μL of 5 mM diethylenetriaminepentaacetic acid (DTPA) was added to the reaction mixture, which was allowed to incubate for another 5 min (DTPA was used to remove non-specifically bound or free ^{64}Cu from the ^{64}Cu-labeled **1** or **2**). The purification of ^{64}Cu-**1** or ^{64}Cu-**2** was carried out by passing the mixture through a Sep-Pak C-18 plus cartridge. After thorough rinsing the cartridge two times with water, the ^{64}Cu-labeled product was eluted out by pure ethanol. The product was firstly analyzed by radio-TLC and then by radio-HPLC to determine the radiochemical purity of the product. Both H_2**1** and H_2**2** were efficiently labeled by ^{64}Cu at 70 °C in 0.4 M NH_4OAc buffer within 30 min. The specific activity of ^{64}Cu-**1** and ^{64}Cu-**2** was in the range of 8.4 – 20.4 GBq/μmol.

Task 6: In Vitro Evaluation of the Radiolabeled Peptides

Serum Stability: An aliquot (*ca.* 40 μCi) of ^{64}Cu-**1** or ^{64}Cu-**2** was added into each of 12 vials containing 100 μL of rat serum. The vials were incubated at 37 ºC in a water bath. At each time point (1, 2, 4 and 24 h), 420 μL of ethanol was added to three of the vials to precipitate the serum proteins. After high speed (14,000 rpm) centrifugation for 5 min, the supernatant was removed and then the pellet was resuspended with 240 μL of 80% ethanol. The suspension was centrifuged again and the supernatant was collected. The supernatants were pooled and then analyzed by radio-HPLC. The dislodged ^{64}Cu from ^{64}Cu-**1** or ^{64}Cu-**2** if any is assumed to be associated with the serum proteins.

The in vitro stability of the ^{64}Cu labeled peptide conjugates was evaluated in rat serum by radio-HPLC. Chromatographic results showed no release of ^{64}Cu from the conjugates over a period of 48 h. This high stability is rendered by the CB-TE2A moiety in the conjugates.

Cell Integrin Receptor-Binding Assay: The $\alpha_v\beta_3$ integrin-binding affinities of ^{64}Cu-**1** and ^{64}Cu-**2**. were determined by a competitive cell-binding assay using ^{125}I-echistatin (PerkinElmer) as the $\alpha_v\beta_3$-specific radioligand. The experiments were performed on U87MG human glioblastoma cells by a previously reported method (*1*, *2*). Briefly, U87MG cells were grown in Dulbecco's modified Eagle medium (DMEM, low glucose) supplemented with 10% (v/v) fetal bovine serum (FBS) at 37ºC with 5% CO_2. Suspended U87MG cells in binding buffer (20 mM Tris, pH 7.4, 150 mM NaCl, 2 mM $CaCl_2$, 1 mM $MgCl_2$, 1 mM $MnCl_2$, 0.1% bovine serum albumin) were seeded on multi-screen DV plates (Millipore) with 2×10^5 cells per well and then incubated with ^{125}I-echistatin (10,000 cpm/well) in the presence of increasing concentrations (0 – 5,000 nM) of c(RGDyK) peptide conjugates for 2 h. The final volume in each well was maintained at 200 μL. At the end of incubation, the unbound ^{125}I-echistatin was removed by filtration and then three times of rinsing with cold binding buffer. The filters were collected and the radioactivity was measured using a γ-counter. The best-fit IC_{50} values (inhibitory concentration where 50% of the ^{125}I-

echistatin bound on U87MG cells are displaced) of c(RGDyK), H_2**1**, and H_2**2** were calculated by fitting the data with nonlinear regression using GraphPad Prism (GraphPad Software, Inc.). Experiments were duplicated with quintuplicate samples. The results are shown in Figure 1.

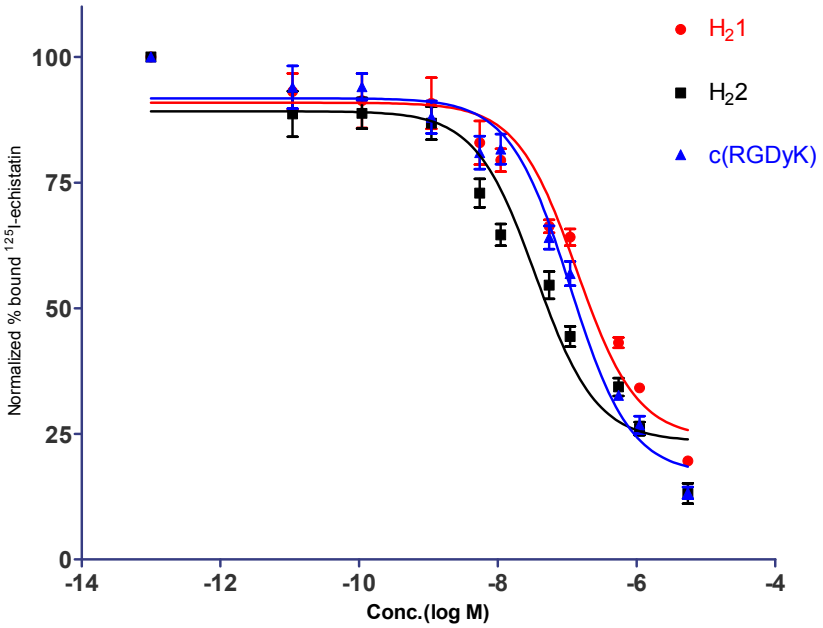

Figure 1. The $\alpha_\upsilon\beta_3$ binding affinities of H_2**1** and H_2**2** measured by a competitive cell-binding assay using U87MG cells where ^{125}I-echistation was employed as $\alpha_\upsilon\beta_3$-specific radioligand. The IC_{50} values of c(RGDyK), H_2**1,** and H_2**2**, were determined to be 110, 139 and 35 nM, respectively (n = 5).

The $\alpha_\upsilon\beta_3$ binding affinities of H_2**1** and H_2**2** were measured by a competitive cell-binding assay using U87MG cells where ^{125}I-echistation was employed as $\alpha_\upsilon\beta_3$-specific radioligand for the competitive displacement.(*3*) The IC_{50} values of c(RGDyK), H_2**1,** and H_2**2**, which represent their concentrations required to displace 50% of the ^{125}I-echistation bound on the U87MG cells, were determined to be 110, 139 and 35 nM, respectively (n = 5). The slightly decreased $\alpha_\upsilon\beta_3$ binding of H_2**1** as compared to c(RGDyK) indicates a minute impact of CB-TE2A on the binding of c(RGDyK) to the $\alpha_\upsilon\beta_3$ integrin. As anticipated, H_2**2** exhibited a strong divalent effect measured by the multivalent enhancement ratio (MVE) calculated by dividing the IC_{50} value of H_2**1** by that of H_2**2** (MVE = 4).(*4*) The distance between the two RGD motifs in H_2**2** is maintained greater than 25 bonds (including the lysine spacers), the minimum spacing length required to realize multivalent binding of RGD motifs to the $\alpha_\upsilon\beta_3$ integrin.(*3*)

Task 7 (Months 12 – 32): In Vivo Evaluation of Radiolabeled Peptides

I. Using c(RGDyK) as a model peptide to validate the multimeric imaging probe design

Tissue Culture and Animal Model: All animal studies were performed in compliance with guidelines set by the UT Southwestern Institutional Animal Care and Use Committee. The PC-3 cell line was obtained from the American Type Culture Collection (ATCC, Manassas, VA). PC-3 cells were cultured in T-media (Invitrogen, Carlsbad, CA) at 37 $^\circ$C in an atmosphere of 5% CO_2 and were passaged at 75 % confluence in P150 plates. T-media was supplemented with 5% Fetal Bovine Serum (FBS) and 1 × Penicillin/Streptomycin. PC-3 cells were harvested from monolayer using PBS and trypsin/EDTA, and suspended in T-media with 5% FBS. The cell suspension was then mixed 1:1 with Matrigel™ and injected

subcutaneously (2.5×10^6 cells per injection, injection volume 100 μL) into both front flanks of SCID mice. After injection, animals were monitored three times a week by general observations. The tumor was noticed to grow in the first week and allowed to grow three weeks to reach a palpable size for microPET-CT imaging and post-PET biodistribution studies. Tumor volume (mm^3) was calculated using the ellipsoid formula ($\pi/6 \times$ length $\times$ width $\times$ depth).

MicroPET-CT Imaging: Small animal PET-CT imaging studies were performed on a Siemens Inveon PET-CT Multimodality System (Siemens Medical Solutions Inc., Knoxville, TN, USA). When the prostate cancer xenografts reached the similar size of approximate 100 mm^3, the tumor-bearing mice were randomized into four groups (n = 3) for the in vivo evaluation of ^{64}Cu-**1,** ^{64}Cu-**2**, ^{64}Cu-**1** with co-injection of c(RGDyK), and ^{64}Cu-**2** with co-injection of c(RGDyK). The dose of c(RGDyK) used for blocking was 10 mg/kg. The injected dose was kept at 100 μCi of ^{64}Cu-activity in 100 μL PBS; and the injected molar amounts of ^{64}Cu-**1** and ^{64}Cu-**2** were maintained at the same level by decay correction.

Ten minutes prior to imaging, the animal was anesthetized using 3% Isofluorane at room temperature until stable vitals were established. Once the animal was sedated, the animal was placed onto the imaging bed under 2% Isofluorane anesthesia for the duration of the imaging. The microCT imaging was acquired at 80 kV and 500 μA with a focal spot of 58 μm. The total rotation of the gantry was 360^o with 360 rotation steps obtained at an exposure time of approximately 235 ms/frame. The images were attained using a CCD readout of 4096 × 3098 with a bin factor of 4 and an average frame of 1. Under low magnification the effective pixel size was 103.03 μm. Total microCT scan time was approximately 6 minutes. CT images were reconstructed with a down sample factor of 2 using Cobra Reconstruction Software. The PET imaging was acquired directly following the acquisition of CT data. The PET tracers were injected intravenously via the tail vein. Static PET scans were performed at 1 h, 4 h, and 24 h post injection (p.i.) for 15 min. PET images were reconstructed using Fourier Rebinning and Ordered Subsets Expectation Maximization 3D (OSEM3D) algorithm. Reconstructed CT and PET images were fused and analyzed using the Siemens Inveon Research Workplace (IRW) software. For quantification, regions of interest were placed in the areas expressing the highest radiotracer activity as determined by visual inspection. The tissues examined include the left and right tumors, the heart, liver, lung, kidney, and muscle. The resulting quantitative data was expressed as percent injected dose per gram of tissue (%ID/g).

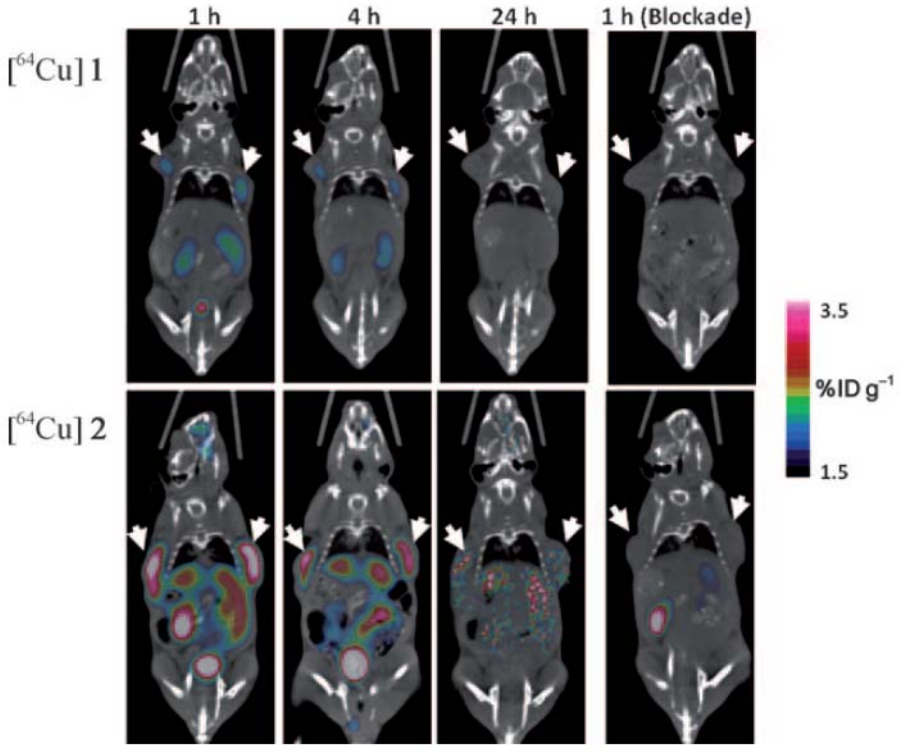

Figure 2. Representative microPET-CT images of PC-3 tumor bearing mice (n = 3) at 1, 4, 24 h after intravenous injection of [^{64}Cu]**1** (upper panel) and [^{64}Cu]**2** (lower panel). Images obtained with co-injection of 10 mg/kg of c(RGDyK) are only shown for 1 h blockade (right). Arrows indicate tumors.

Six SCID mice (6 – 7 weeks old) bearing PC-3 human

prostate cancer xenografts in both front flanks (tumor size: ~ 230 mg) were randomized into two groups (n = 3) for the evaluation of ^{64}Cu-**1** or ^{64}Cu-**2**, which was injected via the tail-vein. As shown in Figure 2, both tumors were visualized by ^{64}Cu-**1** and ^{64}Cu-**2** at 1 h and 4 h p.i., while ^{64}Cu-**2** showed significantly higher PET signal intensity than ^{64}Cu-**1**. At 24 h p.i., the tumors were still clearly visible with ^{64}Cu-**2,** but rather faint with ^{64}Cu-**1**. Due to the fact that the $\alpha_\upsilon\beta_3$ integrin is also expressed in other tissues (e.g. liver, kidneys, stomach, intestines) in young mice but to a lesser extent (personal communications (*5*)), an elevated uptake was observed in those organs with ^{64}Cu-**2** as compared to ^{64}Cu-**1**. The enhanced tumor uptake and retention of ^{64}Cu-**2** may be partially attributed to the difference of in vivo kinetics of ^{64}Cu-**1** and ^{64}Cu-**2**, given the higher molecular weight of ^{64}Cu-**2.** Indeed, ^{64}Cu-**2** was not cleared as efficiently as ^{64}Cu-**1** from kidneys (^{64}Cu-**1**: 94.7 ± 3.6 %ID excreted at 24 h p.i.; ^{64}Cu-**2**: 88.2 ± 4.9 %ID excreted at 24 h p.i.; $p < 0.05$). The $\alpha_\upsilon\beta_3$ binding specificity of ^{64}Cu-**1** and ^{64}Cu-**2** was demonstrated by the PET signal loss (Figure 2: 1 h blockade) in tumors via the co-injection of c(RGDyK) at a dose of 10 mg/kg. The PET images were quantitatively analyzed. The results along with post-PET biodistribution data are presented in Tables 1 – 3

Post-PET Biodistribution: Immediately after the 24 h imaging, the mice were sacrificed and organs of interest were removed, weighed, and counted by a γ-counter. Standards were prepared and counted along with the samples to calculate the percent injected dose per gram (%ID/g) and percent injected dose per organ (%ID/organ).

Table 1. Uptake of Cu-**1** in major organs and tumor determined by PET quantification. Data are presented as %ID/g ± s.d. (n = 3)

Cu-**1**	1 h	1 h (blockade)	4 h	4 h (blockade)	24 h	24 h (blockade)
Lung	0.44 ± 0.04	0.20 ± 0.08	0.17 ± 0.04	0.07 ± 0.03	0.17 ± 0.04	0.02 ± 0.00
Liver	1.37 ± 0.12	0.52 ± 0.17	1.17 ± 0.21	0.46 ± 0.19	0.50 ± 0.05	0.20 ± 0.00
Kidney	2.33 ± 0.15	1.77 ± 0.57	1.80 ± 0.00	1.09 ± 0.27	0.96 ± 0.14	0.47 ± 0.13
Spleen	Not Visible	Not Visible	Not Visible	Not Visible	Not Visible	Not Visible
Heart	0.48 ± 0.05	0.21 ± 0.03	0.12 ± 0.01	0.03 ± 0.00	0.15 ± 0.01	0.03 ± 0.01
Stomach	0.79 ± 0.24	0.25 ± 0.01	0.42 ± 0.08	0.11 ± 0.01	0.31 ± 0.12	0.07 ± 0.00
Muscle	0.00 ± 0.00	0.04 ± 0.04	0.00 ± 0.00	0.01 ± 0.02	0.00 ± 0.00	0.00 ± 0.00
Tumor (left)	1.93 ± 0.15	0.29 ± 0.02	1.87 ± 0.35	0.18 ± 0.07	1.17 ± 0.21	0.12 ± 0.02
Tumor (right)	1.97 ± 0.06	0.33 ± 0.08	1.83 ± 0.21	0.18 ± 0.06	1.03 ± 0.06	0.12 ± 0.01

Table 2. Uptake of Cu-**2** in major organs and tumor determined by PET quantification. Data are presented as %ID/g ± s.d. (n = 3)

Cu-**2**	1 h	1 h (blockade)	4 h	4 h (blockade)	24 h	24 h (blockade)
Lung	0.67 ± 0.01	0.39 ± 0.03	0.48 ± 0.06	0.23 ± 0.01	0.33 ± 0.04	0.14 ± 0.05
Liver	3.10 ± 0.17	1.50 ± 0.14	2.65 ± 0.07	1.45 ± 0.21	2.40 ± 0.10	1.20 ± 0.28
Kidney	4.13 ± 0.29	3.10 ± 0.28	3.10 ± 0.00	1.80 ± 0.28	2.33 ± 0.21	1.40 ± 0.14
Spleen	2.20 ± 0.43	Not Visible	2.2 ± 0.10	Not Visible	2.6 ± 0.10	Not Visible
Heart	0.66 ± 0.02	0.39 ± 0.03	0.44 ± 0.08	0.23 ± 0.01	0.24 ± 0.03	0.12 ± 0.04
Stomach	1.50 ± 0.44	0.57 ± 0.05	1.20 ± 0.14	0.58 ± 0.01	1.20 ± 0.10	0.37 ± 0.05
Muscle	0.47 ± 0.19	0.10 ± 0.11	0.17 ± 0.01	0.03 ± 0.03	0.12 ± 0.07	0.01 ± 0.01
Tumor (left)	2.90 ± 0.35	0.70 ± 0.05	2.35 ± 0.35	0.44 ± 0.02	1.70 ± 0.20	0.31 ± 0.14
Tumor (right)	2.93 ± 0.21	0.72 ± 0.04	2.45 ± 0.07	0.46 ± 0.06	1.73 ± 0.21	0.29 ± 0.13

Table 3. Uptake of Cu-**1** and Cu-**2** in major organs and tumor determined by post-PET biodistribution. Data are presented as %ID/g ± s.d. (n = 3).

	Cu-**1**		Cu-**2**	
	24 h	24 h (blockade)	24 h	24 h (blockade)
Lung	0.29 ± 0.04	0.08 ± 0.01	1.07 ± 0.07	0.62 ± 0.06
Liver	0.31 ± 0.06	0.16 ± 0.02	2.40 ± 0.06	1.70 ± 0.07
Kidney	1.12 ± 0.19	0.65 ± 0.18	2.73 ± 0.03	1.62 ± 0.20
Spleen	0.91 ± 0.15	0.27 ± 0.06	3.20 ± 0.12	0.98 ± 0.08
Heart	0.12 ± 0.02	0.03 ± 0.01	0.49 ± 0.05	0.29 ± 0.01
Stomach	0.50 ± 0.08	0.05 ± 0.01	1.21 ± 0.16	0.34 ± 0.01
Small intestine	0.38 ± 0.04	0.06 ± 0.01	1.39 ± 0.16	0.43 ± 0.06
Large intestine	0.53 ± 0.27	0.07 ± 0.00	1.17 ± 0.37	0.43 ± 0.09
Bone	0.08 ± 0.06	0.05 ± 0.04	0.28 ± 0.03	0.10 ± 0.02
Brain	0.06 ± 0.08	0.00 ± 0.00	0.05 ± 0.00	0.03 ± 0.00
Tumor (left)	1.51 ± 0.09	0.18 ± 0.01	1.72 ± 0.11	0.51 ± 0.05
Tumor (right)	1.26 ± 0.14	0.19 ± 0.03	1.87 ± 0.11	0.47 ± 0.02

These data suggest that the significantly greater uptake and prolonged signal intensity of ^{64}Cu-**2** in tumor reflects the advantages of the scaffolding design of H_2**2,** which affords optimal in vivo kinetics in addition to the anticipated multivalent effects. It must be pointed out that there are two chiral centers in the pendent arms of Cu-**2**, which can statistically give rise to three diastereomers (R/R, S/S, and a meso R/S), although they, if existing, are spectrally indistinguishable in this work. While the purpose of this work is to demonstrate the feasibility of our concept that multivalent imaging probes can be constructed on a bifunctional chelator, an enantiopure isomer should be considered for future clinical applications of this type of multivalent scaffolds. Used as a sample targeting molecule in this work, c(RGDyK) can be obviously replaced by other targeting peptides or small organic molecules for imaging of various diseases or non-invasive cell surface receptor mapping. In summary, we have demonstrated a divalent scaffolding design for targeted imaging probe development. Obviously this concept can be applied to the design of other multivalent scaffolds based on NOTA (1,4,7-triazacyclononane-1,4,7-triacetic acid) or DOTA (1,4,7,10-tetraazacyclododecane-1,4,7,10-tetraacetic acid).

II. Using an arginine-rich cell-permeable peptide (NH_2GR_{11}) to target prostate cancer

Chemical reagents and instrument

All chemicals were of reagent grade and used as received unless otherwise noted. FITC-$NHGR_9$, FITC-$NHGR_{11}$, FITC-$NHGR_{13}$, and DOTA-$NHGR_{11}$ (DOTA: 1,4,7,10-tetraazacyclododecane-1,4,7,10-tetraacetic acid) were synthesized by the Peptide Synthesis Laboratory of the University of Texas Southwestern Medical Center (Dallas, TX). Copper-64 chloride in 0.1N HCl was purchased from the University of Wisconsin-Madison. Milli-Q water (18 MΩ-cm) was obtained from a Millipore Gradient Milli-Q water system (Billerica, MA). All aqueous solutions were prepared with Milli-Q water. Light C-18 Sep-Pak cartridges were purchased from Waters (Milford, MA). Instant thin-layer chromatography (ITLC-SG) plates were purchased from Pall Life Sciences (East Hills, NY).

MALDI-TOF mass spectra were collected on a Voyager-DE™ PRO Biospectrometry Workstation (Applied Biosystems, Foster City, CA). Small animal PET-CT imaging studies were performed on a Siemens Inveon PET-CT Multimodality System (Siemens Medical Solutions Inc., Knoxville, TN).

Cell culture and animal models

All the cell lines used in this work (LNCaP, PZ-HPV-7, DU145, PC3, and H2009) were obtained from the American Type Culture Collection (ATCC, Manassas, VA). Both LNCaP and PC3 cell lines were cultured in T-media (Invitrogen Corporation, Carlsbad, CA) supplemented with 5% FBS and 1× Penicillin/Streptomycin. PZ-HPV-7 (an immortalized normal prostate epithelial cell line) and DU145 cell lines were maintained in PrEGM medium (Lonza, Walkersville, MD) and RPMI1640 medium (ThermoFisher Scientific, US) supplemented with 10% FBS and 1× Penicillin/Streptomycin, respectively. The H2009, a non-small lung cancer, cell line was cultured in RPMI1640 medium supplemented with 5% FBS. All the cell lines were cultured at 37 °C in an atmosphere of 5% CO_2 and passaged at 75 % confluence.

All animal studies were performed in compliance with guidelines set by the UT Southwestern Institutional Animal Care and Use Committee. Male nu/nu nude mice (5 – 7 weeks of age) were purchased from Harlan (Indianapolis, IN), and male SCID mice (6 – 8 weeks of age) were purchased from the UT Southwestern mouse-breeding core (Wakeland Colony). To establish the PC3 tumor xenograft mouse model, PC3 cell suspension was mixed 1:1 with Matrigel (BD Biosciences, Bedford, MA) and then injected subcutaneously (2×10^6 cells per site, injection volume 100 µL) into both flanks of animals. For the H2009 tumor model, the cell suspension was injected subcutaneously (1×10^6 cells per site, injection volume 100 µL) into the back of both shoulders of SCID mice. After injection, the animals were monitored three times a week by general observations. Small PET-CT imaging was performed when the tumors become palpable.

In vitro cell uptake and subcellular localization

To determine the uptake efficiency of CPPs, 1×10^4 cells per well were seeded in 12-well plates and allowed to grow for 24 h. Then a FITC-tagged CCP (5 M) was added and incubated with cells for 30 min. After removal of the medium, the cells were treated with Tryphan Blue (0.4% w/v, Mediatech, Inc., Herndon, VA) to quench the extracellular fluorescence and washed three times with cold PBS. The cells were then lysed with Tris Buffer (50 mM Tris-HCl, pH7.5, 150 mM NaCl, 5 mM EDTA, 1% Triton X100). The fluorescence intensity was measured by SpectraMax M5 (Molecular Devices, Sunnyvale, CA) with an excitation wavelength of 490 nm, an emission wavelength of 530 nm, and a cutoff wavelength of 515 nm. The protein concentration in each well was determined using a BCA protein assay kit (Pierce, Rockford, IL). The uptake efficiency of each CPP was determined by normalizing the fluorescence intensity with the protein concentration and the relative uptake was calculated as compared to that of FITC-$NHGR_{11}$. To determine the subcellular localization of a CPP, after 30 min incubation, the cells were fixed with 4% paraformaldehyde in PBS buffer and then counterstained with 1 µg/mL DAPI (Sigma, St. Louis, MO). Each sample was examined under a fluorescence microscope.

The oligoarginine length effect on the cell uptake efficiency was evaluated using FITC-$NHGR_9$, FITC-$NHGR_{11}$ and FITC-$NHGR_{13}$ in four different human prostate cell lines: PZ-HPV-7, LNCaP, PC3, and DU145. For comparison, the uptake of FITC-$NHGR_{11}$ is set at 1.0. As shown in Figure 3a, after 30 min incubation, FITC-$NHGR_{11}$ displayed much higher uptake efficiency than FITC-$NHGR_9$ and FITC-$NHGR_{13}$ ($p < 0.005$) in all the four cell lines indicating that the intracellular uptake of oligoarginines is greatly affected by the number of the repeating guanidino moiety. Of the three FITC-tagged oligoarginines, FITC-$NHGR_{13}$ showed the lowest uptake in three of the tested cell lines (PZ-HPV-7, PC3, and DU145). In PC3 and DU145, FITC-$NHGR_9$ displayed appreciable uptake values, which are 63% and 65% of that of FITC-$NHGR_{11}$, respectively. Overall, the PZ-HPV-7 and LNCaP cell lines exhibited highly selective internalization of oligoarginines varying with the peptide length.

The subcellular localization of FITC-$NHGR_9$, FITC-$NHGR_{11}$ and FITC-$NHGR_{13}$ in the prostate cancer cell lines was shown in Figure 3b. Apparently, FITC-$NHGR_{11}$ exhibited a higher fluorescent intensity in all the cell lines. The majority of FITC-$NHGR_{11}$ was localized in the cytosol, while in PZ-HPV-7 and PC3 cell lines, nuclear staining with FITC-$NHGR_{11}$ was also seen. Both FITC-$NHGR_9$ and

FITC-NHGR$_{13}$ showed significantly lower fluorescent intensity than FITC-NHGR$_{11}$ in all four tested cell lines, which is consistent with the cell uptake results. Taken together, these data demonstrate the high efficiency and amino acid length-dependent uptake of FITC-NHGR$_{11}$ in various prostate cell lines, which has made FITC-NHGR$_{11}$ as a unique probe for detecting prostate cancer.

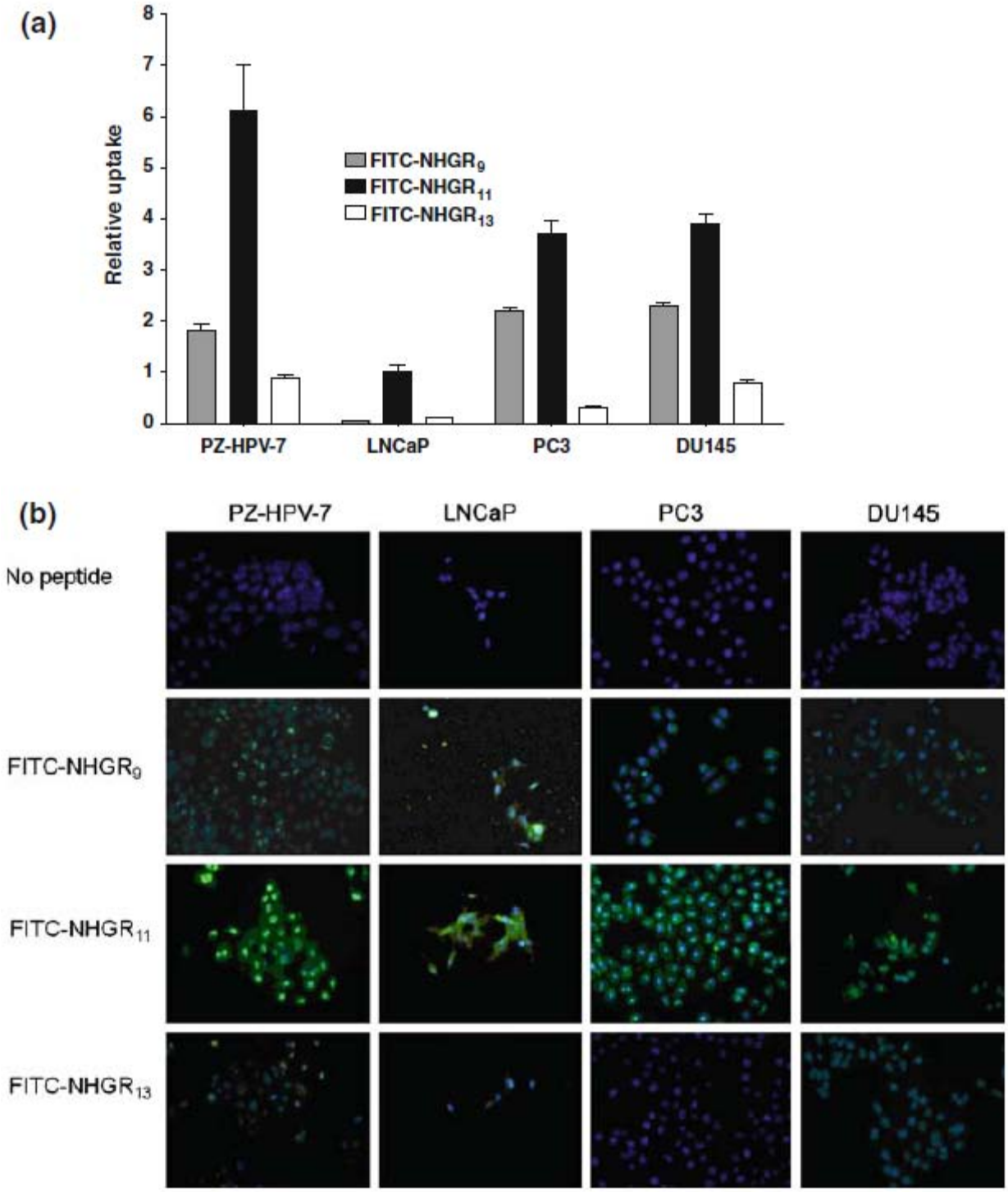

Figure 3. Uptake of FITC-NHGR$_9$, FITC-NHGR$_{11}$, and FITC-NHGR$_{13}$ by prostate cells (PZ-HPV-7, LNCaP, PC3 and DU145). (a): FITC-NHGR$_9$, FITC-NH$_2$GR$_{11}$ and FITC-NH$_2$GR$_{13}$ were incubated with cells for 30 minutes before cell harvesting. Relative FITC intensity was determined by normalizing fluorescence intensity with its protein content and presented as relative level compared to uptake level of FITC-NHGR$_{11}$. *Columns,* mean in triplicate; *bars,* SD. All the experiments were repeated at least twice. (b): cells were incubated with 5 μmol/L of the indicated peptide for 30 minutes. After fixation, cells were

counterstained with DAPI. The cellular distribution of each peptide was visualized with a fluorescence microscope.

Preparation of ^{64}Cu-DOTA-NHGR$_{11}$

To a 1.5 mL vial containing 10 μg DOTA-NHGR$_{11}$ in 200 μL of 0.4 M NH_4OAc solution (pH = 6.5), 2 – 3 mCi of ^{64}Cu in 0.1 M HCl was added. The reaction mixture was vortexed and then incubated at 37 ºC. After 30-min incubation, 5 μL of 5 mM diethylenetriaminepentaacetic acid (DTPA) was added and the reaction mixture was incubated at room temperature for 5 min. The separation of ^{64}Cu-DOTA-NHGR$_{11}$ from ^{64}Cu-DTPA was carried out by passing the reaction mixture through a light C-18 Sep-Pak cartridge. After three times of washings with PBS, the product was eluted with 80% ethanol solution. Radio-TLC analysis was performed on a Rita Star Radioisotope TLC Analyzer (Straubenhardt, Germany) to monitor the radiolabeling reaction using ITLC paper as the plate and 10 mM PBS as the mobile phase. High performance liquid chromatography (HPLC) analysis was conducted to determine the radiochemical purity of the products using a Waters 600 Multisolvent Delivery System equipped with a Waters 2996 Photodiode Array (PDA) detector and an in-line Shell Jr. 2000 radio-detector (Fredericksburg, VA) on a Waters Xterra column (150 × 4.6 mm, 5 μm). The mobile phase was H_2O with 0.1% TFA (solvent A) and acetonitrile with 0.1% TFA (solvent B). The gradient was 5% to 20 % B in 0 – 5 min and 20% to 40% B in 5 – 25 min at 1.0 mL/min flow rate. The cold reference of ^{nat}Cu-DOTA-NHGR$_{11}$ was prepared by reacting 1 mg (0.46 μmol) of DOTA-NHGR$_{11}$ with 62 μg (0.46 μmol) of $CuCl_2$ in 1 mL of 0.4 M NH_4OAc solution at 37 ºC for 1 h. The product was purified by HPLC using the same condition described above and characterized by MALDI-Mass (MALDI-TOF/MS: 2242.1 [M + H^+]). The fraction corresponding to ^{nat}Cu-DOTA-NHGR$_{11}$ was lyophilized and stored for use as cold standard.

The conjugate, DOTA-NHGR$_{11}$, was labeled with ^{64}Cu by incubating with $^{64}Cu^{2+}$ in 0.4 M NH_4OAc buffer (pH = 6.5) at 37 ºC for 30 min. Nonspecifically bound ^{64}Cu was removed in the form of ^{64}Cu-DTPA at the end of the radiolabling procedure. The radiolabeling reaction was monitored by radio-TLC analysis, in which the reaction mixture was sampled on an instant TLC plate that was then developed in PBS buffer. Under the TLC conditions, ^{64}Cu-DOTA-NHGR$_{11}$ stayed at the origin, while ^{64}Cu-DTPA moved to the solvent front. The radiochemical yield was > 90% when 10 μg of the DOTA conjugate was used to label 2 – 3 mCi of ^{64}Cu. The ^{64}Cu-DTPA was removed by passing the reaction mixture through a light C18 Sep-Pak cartridge and three times of washing with PBS. The product, ^{64}Cu-DOTA-NHGR$_{11,}$ could then be efficiently eluted with 80% of ethanol. The radiochemical purity of ^{64}Cu-DOTA-NHGR$_{11}$ was nearly 100% after the Sep-Pak purification as determined by radio-ITLC and radio-HPLC. To confirm the identity of the labeled product, ^{nat}Cu-DOTA-NHGR$_{11}$ was prepared and used as a reference standard. Both ^{64}Cu-DOTA-NHGR$_{11}$ and ^{nat}Cu-DOTA-NHGR$_{11}$ showed a single peak on HPLC (^{64}Cu-DOTA-NHGR$_{11}$: radioactivity detector; ^{nat}Cu-DOTA-NHGR$_{11}$: PDA UV detector) with the same retention time within 14 – 15 min.

Small Animal PET/CT Imaging

When the tumor size reached the range of 50 – 300 mm^3, the tumor-bearing mice were randomized for the PET-CT imaging with ^{64}Cu-DOTA-NHGR$_{11}$. The injected dose was 3.7 MBq of ^{64}Cu-activity in 100 μL of PBS, while the injected molar amount of NH_2GR_{11} was maintained at the same level by decay correction. Ten minutes prior to imaging, the animal was anesthetized using 3% isofluorane at room temperature until stable vitals were established. Once the animal was sedated, it was placed onto the imaging bed under 2% isofluorane anesthesia for the duration of the imaging. The CT imaging was acquired at 80 kV and 500 μA with a focal spot of 58 μm. The total rotation of the gantry was 360° with 360 rotation steps obtained at an exposure time of approximately 235 ms/frame. The images were attained using a CCD readout of 4096 × 3098 with a bin factor of 4 and an average frame of 1. Under low magnification the effective pixel size was 103.03 μm. Total CT scan time was approximately 6 minutes. CT images were reconstructed with a down sample factor of 2 using Cobra Reconstruction Software. The PET imaging was performed directly after the acquisition of CT data. The PET tracer was injected intravenously via the tail vein. Static PET scans

were performed at 1 h, 4 h, and 24 h p.i. for 15 min. PET images at 1 h and 4 h p.i. were reconstructed using Fourier Rebinning and Ordered Subsets Expectation Maximization 3D (OSEM3D) algorithm, while the PET images at 24 h p.i. were reconstructed using OSEM2D. Reconstructed CT and PET images were fused and analyzed using the Siemens Inveon Research Workplace (IRW) software. For quantification, regions of interest were placed in the areas expressing the highest radiotracer activity as determined by visual inspection. The tissues examined include the left and right tumors, heart, liver, lung, kidneys, and muscle. The resulting quantitative data was expressed as percent injected dose per gram of tissue (%ID/g). ***Statistical Analysis***: Quantitative data were expressed as Mean ± SD and then compared using one-way analysis of variance and Student's *t* test. P values < 0.05 were considered statistically significant.

The comparative small animal imaging evaluation of ^{64}Cu-DOTA-NHGR$_{11}$was performed using PC3 and H2009 tumor-bearing SCID mice, which were injected with a similar amount of peptide with respect to the volume of tumor as calculated based on the specificity radioactivity of ^{64}Cu-DOTA-NHGR$_{11}$. The PET-CT imaging acquisition was conducted at 1, 4, and 24 h p.i. (n = 3 at each time point). The representative PET-CT images (transaxial) are presented in Fig 4. Due to the low counts at 24 h p.i. resulted from the clearance and decay of the radiotracer, the PET images at 24 h p.i. were reconstructed by the OSEM2D algorithm instead of OSEM3D that was applied to process the 1 h and 4 h images. As shown in Fig 4, the PC3 tumors on both flanks were clearly visualized by ^{64}Cu-DOTA-NHGR$_{11}$ on PET images at 1 h and 4 h p.i. At 24 h p.i., the PC3 tumors became faint on PET but still with a significant level of signals. In contrast, the H2009 tumors were only visible at 1 h with much lower signal intensity on PET as compared to the PC3 tumors; at 4 h and 24 h p.i., they became not detectable.

The PET images were quantitatively analyzed by the Siemens Inveon Research Workplace (IRW) software. Summarized in Table 4 are the uptake values of ^{64}Cu-DOTA-NHGR$_{11}$ in the regions of interest (tumors [left and right], heart, liver, lung, kidney [left], and muscle) obtained from the imaging quantification. Not surprisingly, ^{64}Cu-DOTA-NHGR$_{11}$ showed nearly identical uptake values in the right and left tumors. The accumulation level of ^{64}Cu-DOTA-NHGR$_{11}$ in the PC3 tumors remained steady out to 24 h p.i. (right tumor: 1.15 ± 0.23 %ID/g at 1 h p.i.; 0.92 ± 0.53 %ID/g at 4 h; 24 h 0.86 ± 0.21 %ID/g at 24 h), whereas its uptake in the H2009 tumors showed an appreciable trend of decreases over time (right tumor: 0.83 ± 0.06 %ID/g at 1 h p.i.; 0.49 ± 0.16 %ID/g at 4 h; 24 h 0.32 ± 0.07 %ID/g at 24 h). Impressively, the uptake ratios of ^{64}Cu-DOTA-NHGR$_{11}$ in PC3 tumor versus muscle at 1 h, 4 h, and 24 h p.i. were 5.06 ± 0.96, 4.87 ± 1.29, and 10.41 ± 6.07, respectively. In other organs, ^{64}Cu-DOTA-NHGR$_{11}$ exhibited a very similar distribution pattern in both tumor-bearing mouse models.

Table 4. PET Quantification data of ^{64}Cu-DOTA-NHGR$_{11}$ in PC3 and H2009 tumor bearing mice at 1 h, 4 h and 24 h p.i. Data is presented as %ID/g ± s.d. (n = 3).

%ID/g	PC3 tumor model			H2009 tumor model		
	1h	4h	24h	1h	4h	24h
Tumor (left)	1.20 ± 0.17	0.89 ± 0.16	0.79 ± 0.32	0.79 ± 0.09	0.45 ± 0.11	0.35 ± 0.04
Tumor (right)	1.15 ± 0.23	0.92 ± 0.53	0.86 ± 0.21	0.83 ± 0.06	0.49 ± 0.16	0.32 ± 0.07
Heart	0.58 ± 0.06	0.52 ± 0.03	0.40 ± 0.06	0.72 ± 0.05	0.43 ± 0.13	0.39 ± 0.03
Liver	9.13 ± 1.75	7.95 ± 1.91	5.03 ± 1.17	8.13 ± 0.12	7.63 ± 0.31	7.20 ± 0.46
Lung	0.59 ± 0.07	0.62 ± 0.10	0.43 ± 0.08	0.55 ± 0.04	0.27 ± 0.05	0.31 ± 0.09
Kidneys	3.93 ± 0.21	3.40 ± 0.00	1.73 ± 0.06	4.27 ± 0.15	4.33 ± 0.35	2.10 ± 0.26
Muscle	0.24 ± 0.06	0.18 ± 0.03	0.09 ± 0.05	0.24 ± 0.03	0.15 ± 0.09	0.09 ± 0.01

With the goal to develop NH_2GR_{11} for specific PET imaging of prostate cancer metastases, we designed and performed a comparative PET-CT imaging experiment by using PC3 and H2009 (a lung cancer model) tumor-bearing mouse models. However due to the availability of ^{64}Cu and the tumor-growth rate

difference between PC3 and H2009, the tumor sizes of PC3 and H2009 could not be ideally matched for this preliminary evaluation. The PC3 tumors were around 100 mm^3 at the time of PET-CT imaging, while the H2009 tumor size was in the range of 100 – 300 mm^3. As shown in Figure 4, the PC3 tumors were clearly visualized with ^{64}Cu-DOTA-NHGR$_{11}$ at 1 h and 4 h p.i., while the H2009 tumors became invisible on PET images after 4 h p.i. The PET imaging quantification further confirmed that the absolute uptake of ^{64}Cu-DOTA-NHGR$_{11}$ in the PC3 tumors was significantly higher than in the H2009 tumors throughout the imaging study, indicating the desired imaging specificity of ^{64}Cu-DOTA-NHGR$_{11}$. The slow clearance of ^{64}Cu-DOTA-NHGR$_{11}$ from the PC3 tumors likely reflects the fact that the radiotracer had been internalized into the tumor cells within 1 h p.i., while the significant clearance of ^{64}Cu-DOTA-NHGR$_{11}$ from the H2009 tumors probably indicates that the radiotracer could not be efficiently internalized into the lung cancer cells. Intriguingly, there are reports that the syndecan-1 expression is lost in lung cancer (*6*, *7*).

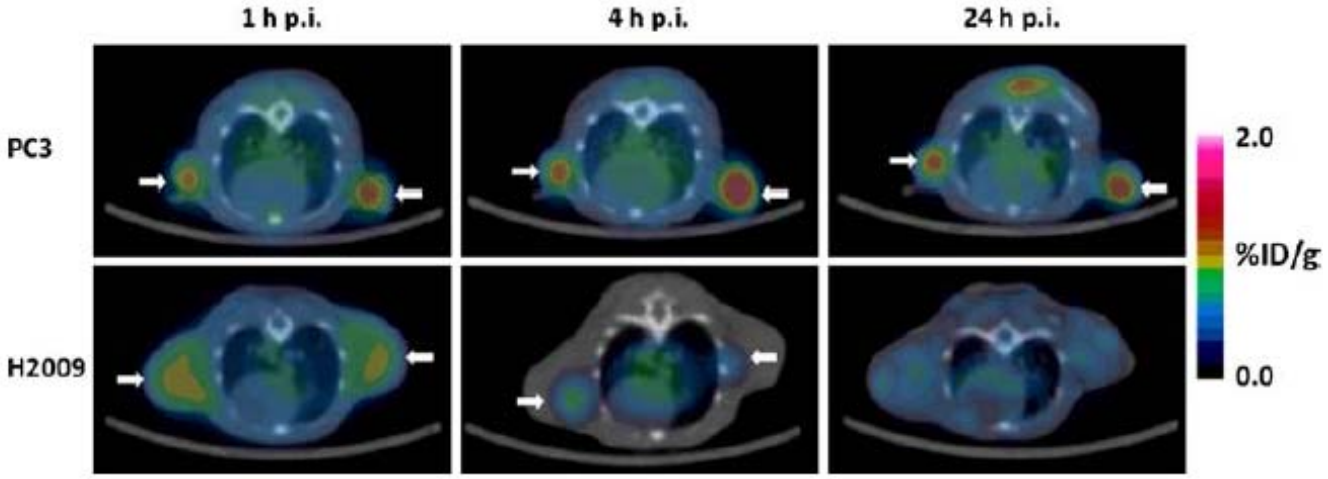

Figure 4. Representative transaxial PET-CT images of ^{64}Cu-DOTA-NHGR$_{11}$ in PC3 and H2009 tumor-bearing mice at 1 h, 4 h, and 24 h p.i. (n = 3). The white arrows indicate tumors.

Part of the research progress has been published on two journal articles:

1. Wei Liu, Guiyang Hao, Michael A. Long, Tiffani Anthony, Jer-Tsong Hsieh, and Xiankai Sun: Imparting Multivalency to a Bifunctional Chelator: A Scaffold Design for Targeted PET Imaging Probes. *Angew. Chem. Int. Ed.* **2009**, 48, 7346 –7349 (in Appendice)

2. Guiyang Hao, Jian Zhou, Yi Guo, Michael A. Long, Tiffani Anthony, Jennifer Stanfield, Jer-Tsong Hsieh, and Xiankai Sun: A cell permeable peptide analog as a potential-specific PET imaging probe for prostate cancer detection. *Amino Acids* **2010**, in press (in Appendice)

Key Research Accomplishments

1. In *Angew. Chem. Int. Ed.* paper, we reported the design and synthesis of the proposed multifunctional chelators and demonstrated the feasibility of building multivalent imaging probes from a bifunctional chelator. Using c(RGDyK) as a model targeting molecule, we showed that a targeted divalent PET imaging probe could be constructed for prostate cancer detection. Obviously this concept can be applied to the design of other multivalent scaffolds based on NOTA (1,4,7-triazacyclononane-1,4,7-triacetic acid) or DOTA (1,4,7,10-tetraazacyclododecane-1,4,7,10-tetraacetic acid).

2. In the *Amino Acids* paper, we demonstrated the potential of using $NHGR_{11}$ to develop specific PET imaging probes for distant prostate cancer metastases by both in vitro and in vivo evaluations performed with FITC-NHGR11 and ^{64}Cu-DOTA-NHGR11.

Reportable Outcomes

1. Liu et al. *Angew. Chem. Int. Ed.* **2009**, 48, 7346 –7349
2. Hao et al. *Amino Acids* **2010**, in press

Conclusions

By two-year work, we have successfully developed an approach to impart multivalency to a bifunctional chelator for targeted PET imaging probe design. This type of multivalent scaffolds features a chelator that forms a stable and neutral complex with a radiometal and multiple functional groups for multimeric presentation of targeting molecules. A bivalent scaffold was synthesized and coupled with an integrin $\alpha_v\beta_3$ targeting ligand, c(RGDyK), to afford a ^{64}Cu-labeled divalent probe. The in vitro and in vivo evaluation clearly demonstrated the divalent probe with the anticipated multivalent effect as compared to its monomeric counterpart. In addition, we have further verified the imaging specificity of ^{64}Cu-DOTA-$NHGR_{11}$ for prostate cancer detection.

References

(1) Cai, W., Zhang, X., Wu, Y., and Chen, X. (2006) A thiol-reactive 18F-labeling agent, N-[2-(4-18F-fluorobenzamido)ethyl]maleimide, and synthesis of RGD peptide-based tracer for PET imaging of alpha v beta 3 integrin expression. *J Nucl Med 47*, 1172-80.

(2) Wu, Y., Zhang, X., Xiong, Z., Cheng, Z., Fisher, D. R., Liu, S., Gambhir, S. S., and Chen, X. (2005) microPET imaging of glioma integrin {alpha}v{beta}3 expression using (64)Cu-labeled tetrameric RGD peptide. *J Nucl Med 46*, 1707-18.

(3) Li, Z. B., Cai, W., Cao, Q., Chen, K., Wu, Z., He, L., and Chen, X. (2007) (64)Cu-labeled tetrameric and octameric RGD peptides for small-animal PET of tumor alpha(v)beta(3) integrin expression. *J Nucl Med 48*, 1162-71.

(4) Montet, X., Funovics, M., Montet-Abou, K., Weissleder, R., and Josephson, L. (2006) Multivalent effects of RGD peptides obtained by nanoparticle display. *J Med Chem 49*, 6087-93.

(5) *Unpublished data in Dr. Shuang Liu's Laboratory at Purdue University, Indiana, USA.*

(6) Chen, D., Adenekan, B., Chen, L., Vaughan, E. D., Gerald, W., Feng, Z., and Knudsen, B. S. (2004) Syndecan-1 expression in locally invasive and metastatic prostate cancer. *Urology 63*, 402-7.

(7) Nackaerts, K., Verbeken, E., Deneffe, G., Vanderschueren, B., Demedts, M., and David, G. (1997) Heparan sulfate proteoglycan expression in human lung-cancer cells. *Int J Cancer 74*, 335-45.

Imaging Probes

DOI: 10.1002/anie.200903556

Imparting Multivalency to a Bifunctional Chelator: A Scaffold Design for Targeted PET Imaging Probes**

*Wei Liu, Guiyang Hao, Michael A. Long, Tiffani Anthony, Jer-Tsong Hsieh, and Xiankai Sun**

Positron emission tomography (PET) has become a standard clinical practice in the diagnostic or prognostic imaging of cancer, mainly owing to the great success of [^{18}F]FDG (2-deoxy-2-^{18}F-fluoro-D-glucose) for non-invasive detection of glucose uptake in tumors.[1] Currently ^{11}C and ^{18}F are the most commonly used PET nuclides for the development of PET imaging probes. However, the short half-lives of these two radioisotopes (^{11}C $t_{1/2} = 20.3$ m, ^{18}F $t_{1/2} = 109$ m) limit their applications to biomolecules with relatively fast in vivo biodistribution kinetics, and the chemical procedures to incorporate these isotopes must be carried out in the proximity of a biomedical cyclotron. Among nonstandard PET nuclides, ^{64}Cu ($t_{1/2} = 12.7$ h; β^+ 0.653 MeV, 17.4%) has drawn considerable interest in PET research owing to its low positron range, commercial availability, and reasonably long decay half-life. Such characteristics could enable a variety of imaging applications involving peptides, antibodies or their fragments, and nanoparticles.[2,3]

It has been demonstrated that creation of multimers of a targeting molecule on one scaffold can efficiently improve cell-specific binding affinity by several orders of magnitude.[3] As such, various approaches have been reported to exploit multivalent scaffolds for the construction of molecular imaging probes.[4–10] However, their chemistries are often complicated and become even more so when a bifunctional chelator (BFC) must be attached to a separately multimerized construct in order to introduce a metal radionuclide for nuclear imaging.

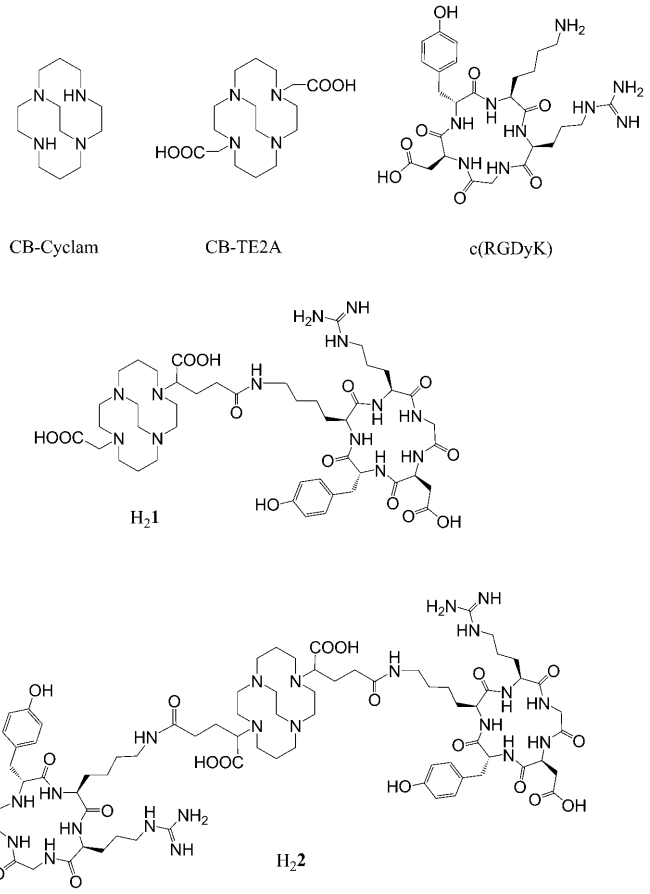

Scheme 1. Chemical structures of relevant compounds

Herein we present an approach to take advantage of the pendent arms of the commonly used BFCs to build simplified but potentially versatile multivalent scaffolds for multimeric presentation of targeting molecules. This type of multivalent scaffold features a chelator that forms a stable and neutral complex with a radiometal and multiple functional groups for the anchoring of targeting molecules. If required by in vivo pharmacokinetics, poly(ethylene glycol) (PEG) chains can be introduced between the chelate and targeting moieties.

To test the rationale of our design, we use a cyclic RGD peptide (c(RGDyK),[5,11] a well-validated $\alpha_v\beta_3$ integrin ligand, for the construction of a divalent PET imaging probe from a chelate known to have a high affinity for ^{64}Cu (CB-TE2A, Scheme 1). The divalent probe is anticipated to have a prolonged biological half-life and enhanced specific binding and retention in tissues expressing the $\alpha_v\beta_3$ integrin.

[*] W. Liu, G. Hao, M. A. Long, T. Anthony, X. Sun
Department of Radiology and Advanced Imaging Research Center
University of Texas Southwestern Medical Center
Dallas, TX 75390-8542 (USA)
Fax: (+1) 214-645-2885
E-mail: xiankai.sun@utsouthwestern.edu
J.-T. Hsieh
Department of Urology
University of Texas Southwestern Medical Center
Dallas, TX 75390-9110 (USA)

[**] This work was partially supported by a USAMRMC grant (W81XWH-08-1-0305) and two NIH grants (P01 DK058398; U24 CA126608). The authors acknowledge the generous support of a private donor that allowed the purchase of the Inveon PET-CT system. The c(RGDyK) peptide was provided by Dr. Xiaoyuan Chen at Stanford University

Supporting information for this article is available on the WWW under http://dx.doi.org/10.1002/anie.200903556.

The stability of the metal complex is of critical importance in the design of a metal radiopharmaceutical. CB-TE2A forms one of the most stable complexes with ^{64}Cu,[12] and the Cu^{II}-CB-TE2A complex is more resistant to reductive metal loss than are other tetramacrocyclic complexes.[13] However, its stability with ^{64}Cu may be reduced when used as a BFC in which one of the carboxylate groups is converted to an amide for conjugation to a targeting molecule,[14] leading to a positive charge on the ^{64}Cu moiety. To avoid this potential problem, we choose α-bromoglutaric acid-1-*tert*-butyl ester-5-benzyl ester (**3**) for the alkylation of CB-cyclam, which allows selective deprotection of the carboxylate groups by two separate procedures to conjugate with c(RGDyK) through the peripheral carboxylates to afford H_2**1** and H_2**2**, respectively. As such, the unique feature of CB-TE2A is preserved in the conjugates, in which the two inner carboxylates can form a neutral octahedral complex with $^{64}Cu^{II}$ along with the four nitrogen atoms of the macrocycle.

To evaluate the anticipated multivalent effect, a recently reported CB-TE2A analogue[15] was also synthesized and coupled with c(RGDyK) to form a monovalent CB-TE2A-RGD conjugate (H_2**1**) as a control for comparison. Scheme 2 shows the synthetic routes to H_2**1** and H_2**2**. The multiple-step synthetic route involves three parts: 1) synthesis of orthogonally protected compounds **5** and **7;** 2) formation of NHS-activated ester intermediates **6** and **9** after selective deprotection of the peripheral carboxylate groups (NHS = *N*-hydroxysuccinimide); and 3) conjugation of c(RGDyK) to the NHS esters followed by acid deprotection of the inner carboxylate groups to form the products H_2**1** and H_2**2**. Alkylation of CB-cyclam by **3** was asynchronous at the two nonbridged nitrogen atoms, with the monoalkylation product **4** predominating at room temperature (35–55% yield even in the presence of excess of **3**).[15] In comparison, the dialkylated product **7** was only formed at elevated temperatures. At 50 °C using two equivalents of **3** to CB-cyclam, only 20–45% of **7** was found, and it was always accompanied by the monoalkylation product. Although **7** was difficult to elute from silica gel using common organic solvents, a good separation was obtained by adding 5–10% isopropyl amine in ethyl acetate. It is noteworthy that the debenzylation of the peripheral carboxylate groups catalyzed by 10% Pd/C in a hydrogen atmosphere always resulted in formation of the corresponding esters if the reaction was carried out in an alcohol solvent. This finding is likely due to the "proton sponge" nature of the CB-cyclam core that induces transesterification during debenzylation. No clean debenzylization could be accomplished in either methanol or ethanol, even in the presence of formic acid as described in literature.[15] However, THF/H_2O (1:1) successful circumvented this problem and afforded debenzylation products in quantitative yield. These were then activated by NHS and conjugated to c(RGDyK) in the presence of ten equivalents *N*,*N*-diisopropylethylamine (DIPEA). After HPLC purification, H_2**1** and H_2**2** were obtained by removal of the *tert*-butyl groups using 95% trifluoroacetic acid (TFA; see the Supporting Information for details).

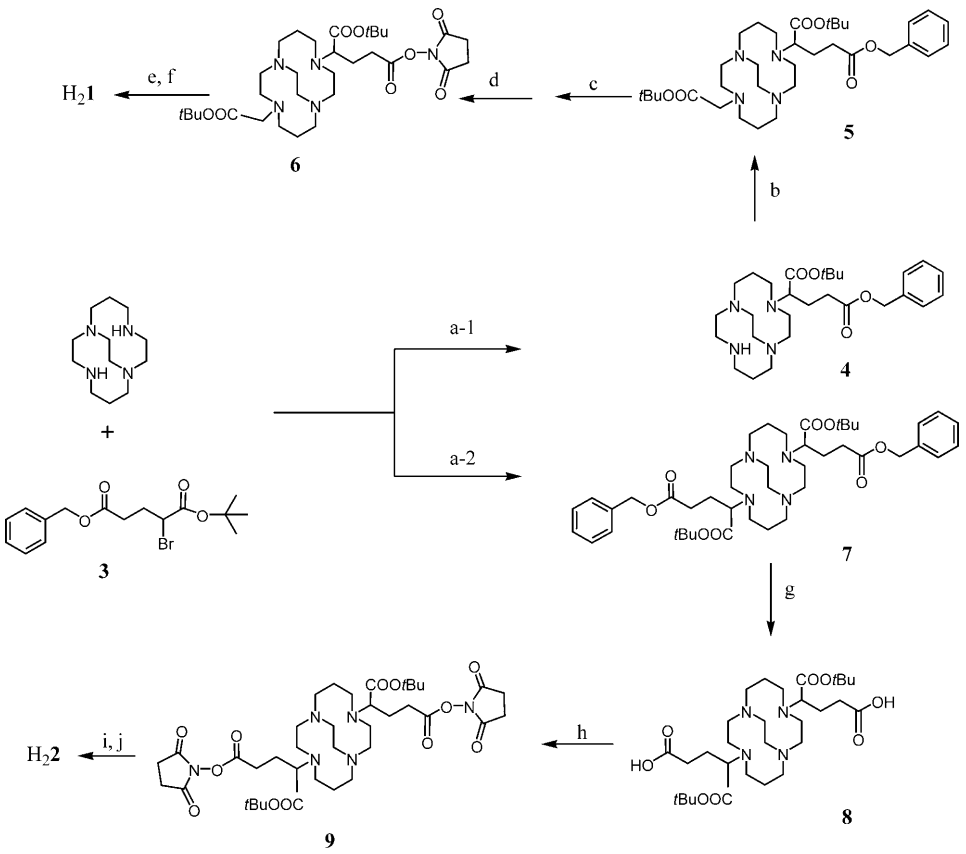

Scheme 2. Synthesis of H_2**1** and H_2**2**. Reagents: a-1, a-2) CH_3CN, K_2CO_3; b) $BrCH_2COOtBu$, CH_3CN, K_2CO_3; c, g) 10% Pd/C, THF/H_2O; d, h) MeCN, NHS, 1-ethyl-3-(3-dimethylaminopropyl)carbodiimide (EDC); f, i) c(RGDyK), DIPEA, DMF; e, j) 95% TFA.

Both H_2**1** and H_2**2** were efficiently labeled by ^{64}Cu at 70 °C in 0.4 M NH_4OAc buffer within 30 min. The specific activity of [^{64}Cu]**1** and [^{64}Cu]**2** was in the range of 8.4–20.4 GBq μmol^{-1}. The in vitro stability of the ^{64}Cu-labeled peptide conjugates was evaluated in rat serum by radio-HPLC. Chromatographic results showed no release of ^{64}Cu from the conjugates over a period of 48 h. This high stability is attributed to the CB-TE2A moiety in the conjugates. The $\alpha_v\beta_3$ binding affinities of H_2**1** and H_2**2** were measured by a competitive cell-binding assay using U87MG cells in which ^{125}I-echistation was employed as $\alpha_v\beta_3$-specific radioligand for

competitive displacement.[5] The U87MG cell line was chosen because the $\alpha_v\beta_3$ integrin density on the cell surface was the highest among the solid tumor cell lines that have been assessed.[16] The IC_{50} values of c(RGDyK), H_2**1**, and H_2**2**, which represent their concentrations required to displace 50% of the ^{125}I-echistation bound on the U87MG cells, were determined to be 110, 139, and 35 nM, respectively ($n=5$). The slightly decreased $\alpha_v\beta_3$ binding of H_2**1** as compared to c(RGDyK) indicates a minute impact of CB-TE2A on the binding of c(RGDyK) to the $\alpha_v\beta_3$ integrin. As anticipated, H_2**2** exhibited a strong divalent effect measured by the multivalent enhancement ratio (MVE) calculated by dividing the IC_{50} value of H_2**1** by that of H_2**2** (MVE = 4).[6] The distance between the two RGD motifs in H_2**2** is greater than 25 bonds (including the lysine spacers), the minimum spacing length required to realize multivalent binding of RGD motifs to the $\alpha_v\beta_3$ integrin.[5] It is noteworthy that as a downstream effect of multivalent binding, oligomerization of cell-surface receptors could initiate cellular internalization events, which might further enhance the specific accumulation in the target tissues.[17]

In vivo small-animal imaging studies were performed on a Siemens Inveon PET-CT multimodality system. Six SCID mice (6–7 weeks old) bearing PC-3 human prostate cancer xenografts in both front flanks (tumor size ca. 230 mg) were randomized into two groups ($n=3$) for the evaluation of [^{64}Cu]**1** or [^{64}Cu]**2**, which was injected into the tail vein. As shown in Figure 1, both tumors were visualized by [^{64}Cu]**1** and [^{64}Cu]**2** at 1 and 4 h post injection (p.i.), while [^{64}Cu]**2** showed a significantly stronger PET signal than [^{64}Cu]**1** at all time points. At 24 h p.i., the tumors were still clearly visible with [^{64}Cu]**2** but were rather faint with [^{64}Cu]**1**. Owing to the fact that the $\alpha_v\beta_3$ integrin is also expressed in other tissues (e.g. liver, kidneys, stomach, intestines) in young mice, but to a lesser extent (personal communications[18]), an elevated uptake was observed in those organs with [^{64}Cu]**2** as compared to [^{64}Cu]**1**. The enhanced tumor uptake and retention of [^{64}Cu]**2** may be partially attributed to the difference of in vivo kinetics of [^{64}Cu]**1** and [^{64}Cu]**2**, given the higher molecular weight of [^{64}Cu]**2**. Indeed, [^{64}Cu]**2** was not cleared as efficiently as [^{64}Cu]**1** from kidneys ([^{64}Cu]**1** 94.7 ± 3.6% ID excreted at 24 h p.i.; [^{64}Cu]**2** 88.2 ± 4.9% ID excreted at 24 h p.i.; $p<0.05$). The $\alpha_v\beta_3$ binding specificity of [^{64}Cu]**1** and [^{64}Cu]**2** was demonstrated by signal loss (Figure 1: 1 h blockade) in tumors after co-injection of c(RGDyK) at a dose of 10 mg kg^{-1}. The quantitative PET image data and post-PET biodistribution data are presented in Table 1 and Tables S1–S3 (see the Supporting Information for details).

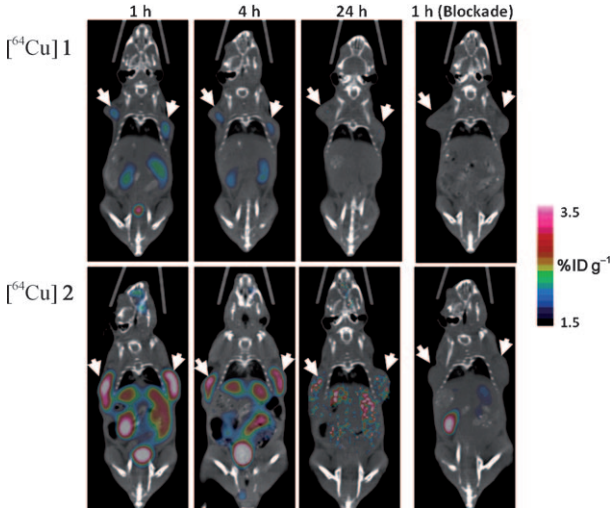

Figure 1. Representative microPET-CT images of PC-3 tumor bearing mice ($n=3$) at 1, 4, 24 h after intravenous injection of [^{64}Cu]**1** (upper panel) and [^{64}Cu]**2** (lower panel). Images obtained with co-injection of 10 mg kg^{-1} of c(RGDyK) are only shown for 1 h blockade (right). Arrows indicate tumors.

Table 1: Tumor uptake of [^{64}Cu]**1** and [^{64}Cu]**2** as determined from PET imaging quantitation and post-PET biodistribution. Data are presented as %ID g^{-1} ± standard deviation ($n=3$).[a]

	1 h PET	4 h PET	24 h PET	24 h Post-PET	1 h PET (blockade)
[^{64}Cu]**1**	1.95 ± 0.10	1.85 ± 0.26	1.10 ± 0.15	1.39 ± 0.17	0.31 ± 0.05
[^{64}Cu]**2**	2.92 ± 0.26	2.40 ± 0.22	1.72 ± 0.18	1.79 ± 0.13	0.71 ± 0.04

[a] For [^{64}Cu]**2**, $p<0.05$ for all times.

The significantly greater uptake and prolonged signal intensity of [^{64}Cu]**2** in tumors reflects the advantages of the scaffolding design of H_2**2**, which affords optimal in vivo kinetics in addition to the anticipated multivalent effects. It should be pointed out that there are two chiral centers in the pendent arms of Cu**2**, which should statistically give rise to three diastereomers (*R*/*R*, *S*/*S*, and a meso *R*/*S*), even though they could not be distinguished by the techniques used herein. While the purpose of this work is to demonstrate the feasibility of building multivalent imaging probes from a bifunctional chelator, an enantiopure isomer of **3** should be considered for future clinical applications of this type of multivalent scaffold. Used as a sample targeting molecule herein, c(RGDyK) can obviously be replaced with other targeting peptides or small organic molecules for imaging of various diseases or non-invasive cell-surface receptor mapping. In summary, we have demonstrated a divalent scaffolding design for targeted imaging probe development. Obviously this concept can be applied to the design of other multivalent scaffolds based on NOTA (1,4,7-triazacyclononane-1,4,7-triacetic acid) or DOTA (1,4,7,10-tetraazacyclododecane-1,4,7,10-tetraacetic acid).

Received: June 30, 2009
Revised: July 18, 2009
Published online: September 1, 2009

Keywords: chelates · imaging agents · multivalent effect · radiochemistry

[1] M. Allen-Auerbach, W. A. Weber, *Oncologist* **2009**, *14*, 369.
[2] R. Rossin, S. Muro, M. J. Welch, V. R. Muzykantov, D. P. Schuster, *J. Nucl. Med.* **2008**, *49*, 103.
[3] R. Haubner, H. J. Wester, *Curr. Pharm. Des.* **2004**, *10*, 1439.

[4] A. Almutairi, R. Rossin, M. Shokeen, A. Hagooly, A. Ananth, B. Capoccia, S. Guillaudeu, D. Abendschein, C. J. Anderson, M. J. Welch, J. M. Frechet, *Proc. Natl. Acad. Sci. USA* **2009**, *106*, 685.
[5] Z. B. Li, W. Cai, Q. Cao, K. Chen, Z. Wu, L. He, X. Chen, *J. Nucl. Med.* **2007**, *48*, 1162.
[6] X. Montet, M. Funovics, K. Montet-Abou, R. Weissleder, L. Josephson, *J. Med. Chem.* **2006**, *49*, 6087.
[7] I. Dijkgraaf, J. A. Kruijtzer, S. Liu, A. C. Soede, W. J. Oyen, F. H. Corstens, R. M. Liskamp, O. C. Boerman, *Eur. J. Nucl. Med. Mol. Imaging* **2007**, *34*, 267.
[8] I. Dijkgraaf, A. Y. Rijnders, A. Soede, A. C. Dechesne, G. W. van Esse, A. J. Brouwer, F. H. Corstens, O. C. Boerman, D. T. Rijkers, R. M. Liskamp, *Org. Biomol. Chem.* **2007**, *5*, 935.
[9] M. Janssen, W. J. Oyen, L. F. Massuger, C. Frielink, I. Dijkgraaf, D. S. Edwards, M. Radjopadhye, F. H. Corstens, O. C. Boerman, *Cancer Biother. Radiopharm.* **2002**, *17*, 641.
[10] S. Liu, *Mol. Pharm.* **2006**, *3*, 472.
[11] W. Cai, S. S. Gambhir, X. Chen, *Methods Enzymol.* **2008**, *445*, 141.
[12] X. Sun, M. Wuest, G. R. Weisman, E. H. Wong, D. P. Reed, C. A. Boswell, R. Motekaitis, A. E. Martell, M. J. Welch, C. J. Anderson, *J. Med. Chem.* **2002**, *45*, 469.
[13] K. S. Woodin, K. J. Heroux, C. A. Boswell, E. H. Wong, G. R. Weisman, W. Niu, S. A. Tomellini, C. J. Anderson, L. N. Zakharov, A. L. Rheingold, *Eur. J. Inorg. Chem.* **2005**, 4829.
[14] M. Woods, P. Caravan, C. F. Geraldes, M. T. Greenfield, G. E. Kiefer, M. Lin, K. McMillan, M. I. Prata, A. C. Santos, X. Sun, J. Wang, S. Zhang, P. Zhao, A. D. Sherry, *Invest. Radiol.* **2008**, *43*, 861.
[15] C. A. Boswell, C. A. Regino, K. E. Baidoo, K. J. Wong, A. Bumb, H. Xu, D. E. Milenic, J. A. Kelley, C. C. Lai, M. W. Brechbiel, *Bioconjugate Chem.* **2008**, *19*, 1476.
[16] X. Zhang, Z. Xiong, Y. Wu, W. Cai, J. R. Tseng, S. S. Gambhir, X. Chen, *J. Nucl. Med.* **2006**, *47*, 113.
[17] J. E. Gestwicki, C. W. Cairo, L. E. Strong, K. A. Oetjen, L. L. Kiessling, *J. Am. Chem. Soc.* **2002**, *124*, 14922.
[18] S. Liu, unpublished results.

Amino Acids
DOI 10.1007/s00726-010-0515-5

ORIGINAL ARTICLE

A cell permeable peptide analog as a potential-specific PET imaging probe for prostate cancer detection

Guiyang Hao · Jian Zhou · Yi Guo · Michael A. Long · Tiffani Anthony · Jennifer Stanfield · Jer-Tsong Hsieh · Xiankai Sun

Received: 25 November 2009 / Accepted: 4 February 2010

Abstract Non-invasive detection of prostate cancer or metastases still remains a challenge in the field of molecular imaging. In our recent work of screening arginine- or lysine-rich peptides for intracellular delivery of a therapeutic agent into prostate cancer cells, an arginine-rich cell permeable peptide (NH_2GR_{11}) was found with an unexpectedly preferential uptake in prostate cancer cell lines. The goal of this work was to develop this peptide as a positron emission tomography (PET) imaging probe for specific detection of distant prostate cancer metastases. The optimal length of arginine-rich peptides was evaluated by the cell uptake efficiency of three fluorescein isothiocyanate (FITC)-tagged oligoarginines ($NHGR_9$, $NHGR_{11}$, and $NHGR_{13}$) in four human prostate cell lines (LNCaP, PZ-HPV-7, DU145, and PC3). Of the three oligoarginines, NH_2GR_{11} showed the highest cell uptake and internalization efficiency with its subcellular localization in cytosol. The biodistribution of FITC-$NHGR_9$, FITC-$NHGR_{11}$, and FITC-$NHGR_{13}$ performed in control nude mice displayed the unique preferential accumulation of FITC-$NHGR_{11}$ in the prostate tissue. Further in vivo evaluation of FITC-$NHGR_{11}$ in PC3 tumor-bearing nude mice revealed elevated uptake of this peptide in tumors as compared to other organs. In vivo pharmacokinetics evaluated with ^{64}Cu-labeled NH_2GR_{11} showed that the peptide was rapidly cleared from the blood ($t_{1/2} = 10.7$ min) and its elimination half-life was 17.2 h. The PET imaging specificity of ^{64}Cu-labled NH_2GR_{11} was demonstrated for the detection of prostate cancer in a comparative imaging experiment using two different human cancer xenograft models.

Keywords PET · Prostate cancer · Cell permeable peptide · ^{64}Cu

G. Hao · Y. Guo · M. A. Long · T. Anthony
Department of Radiology, University of Texas Southwestern Medical Center, Dallas, TX 75390, USA

J. Zhou · J. Stanfield · J.-T. Hsieh (✉)
Department of Urology, University of Texas Southwestern Medical Center, Dallas, TX 75390, USA
e-mail: JT.Hsieh@UTSouthwestern.edu

X. Sun (✉)
Department of Radiology, Advanced Imaging Research Center, University of Texas Southwestern Medical Center, Dallas, TX 75390, USA
e-mail: Xiankai.Sun@UTSouthwestern.edu

Introduction

Currently the most commonly used positron emission tomography (PET) probe, 2-^{18}F-fluoro-2-deoxy-D-glucose (^{18}F-FDG), is not so successful at identifying localized prostate cancer or distal metastases because the prostate is in the close proximity of the bladder, where the FDG is cleared, and the prostate cancer cells are inherently not glucose avid (Shreve et al. 1996; Etchebehere et al. 2002; Gambhir 2002). To date, various PET tracers have been introduced for prostate cancer imaging based on different molecular mechanisms (Emonds et al. 2009). To name a few, ^{11}C- or ^{18}F-labeled choline showed promising results of detecting primary and metastatic prostate cancer but with inconsistent findings in densely sclerotic bone lesions (Hara et al. 1998; Maeda et al. 2006; Vees et al. 2007; Giovacchini et al. 2008); ^{11}C- or ^{18}F-labeled acetate was reported with potential to detect local recurrences and regional lymph node metastases (Oyama et al. 2002; Albrecht et al. 2007; Ponde et al. 2007); 3′-^{18}F-fluorothymidine was used for monitoring the therapeutic effect of

Published online: 11 March 2010

androgen ablation therapy in prostate cancer (Oyama et al. 2004); 16β-^{18}F-fluoro-5α-dihydrotesterone was employed to detect prostate cancer metastases and access androgen receptor expression in vivo (Larson et al. 2004); and radiolabeled peptides have been exploited for specific prostate cancer imaging by targeting specific surface markers or receptors (Rogers et al. 2003; Chen et al. 2004a, b; Schuhmacher et al. 2005; Yang et al. 2006; Zhang et al. 2006). However, the role of PET in the diagnosis of prostate cancer, either localized diseases or distal metastases, has not been established (Beheshti et al. 2009; Bouchelouche et al. 2009). Prostate cancer metastases, especially in their early stage, display the dormant characteristics of prostate cancer with relatively small size as compared to metastases of other carcinomas, such as breast and lung cancer (Fogelman et al. 2005; Langsteger et al. 2006). This represents a great challenge in the non-invasive detection of prostate cancer and its metastases. As such, it is highly desirable to develop specific PET imaging probes based on different molecular mechanisms.

Cell permeable peptides (CPPs) known as delivery vehicles that can cross cell membranes have been extensively used for intracellular delivery of varieties of bioactive cargos (Bucci et al. 2000; Gratton et al. 2003). Of the commonly used CPPs, arginine-rich CPPs including HIV-Tat peptides and oligoarginines have been reported with high internalization efficacy likely because their guanidine moiety can form divalent hydrogen-bonds with phosphates, sulfates, and carboxylates on cellular components (Rothbard et al. 2004; Sakai et al. 2005). In an effort to deliver a therapeutic peptide sequence derived from the proline-rich domain of DOC-2/DAB2 for prostate cancer treatment, we found out a polyarginine peptide (NH_2GR_{11}) with an unexpectedly preferential uptake in several prostate cancer cell lines (Zhou et al. 2006), which initiated the work presented in this paper. Two experiments were designed to verify whether the uptake preference is a unique feature of NH_2GR_{11} and whether it displays similar uptake specificity to prostate cancer in vivo. One was performed with three oligoarginines differing in the number of the repeating arginine units ($n = 9$, 11, and 13), which were labeled with a fluorescent dye (FITC: fluorescein isothiocyanate). NH_2GR_{11} was found with significantly higher uptake than NH_2GR_9 and NH_2GR_{13} in four human prostate cancer cell lines and in both normal and prostate cancer-bearing mouse models. Subsequently, a comparative PET-CT imaging study using prostate and lung cancer xenograft mouse models was carried out to test the specificity of using NH_2GR_{11} to image prostate cancer in vivo when labeled with ^{64}Cu ($t_{1/2} = 12.7$ h; β^+: 0.653 meV, 17.4%), a positron emitter. Our preliminary results demonstrate the potential of NH_2GR_{11} to be developed as a specific imaging probe for the detection of prostate cancer metastases.

Materials and methods

Chemical reagents and instrument

All chemicals were of reagent grade and used as received unless otherwise noted. FITC-$NHGR_9$, FITC-$NHGR_{11}$, FITC-$NHGR_{13}$, and DOTA-$NHGR_{11}$ (DOTA: 1,4,7,10-tetraazacyclododecane-1,4,7,10-tetraacetic acid) were synthesized by the Peptide Synthesis Laboratory of the University of Texas Southwestern Medical Center (Dallas, TX). Copper-64 chloride in 0.1 N HCl was purchased from the University of Wisconsin-Madison. Milli-Q water (18 MΩ cm) was obtained from a Millipore Gradient Milli-Q water system (Billerica, MA). All aqueous solutions were prepared with Milli-Q water. Light C-18 Sep-Pak cartridges were purchased from Waters (Milford, MA). Instant thin-layer chromatography (ITLC-SG) plates were purchased from Pall Life Sciences (East Hills, NY).

MALDI-TOF mass spectra were collected on a Voyager-DE™ PRO Biospectrometry Workstation (Applied Biosystems, Foster City, CA). Small animal PET-CT imaging studies were performed on a Siemens Inveon PET-CT Multimodality System (Siemens Medical Solutions Inc., Knoxville, TN).

Cell culture and animal models

All the cell lines used in this work (LNCaP, PZ-HPV-7, DU145, PC3, and H2009) were obtained from the American Type Culture Collection (ATCC, Manassas, VA). Both LNCaP and PC3 cell lines were cultured in T-media (Invitrogen Corporation, Carlsbad, CA) supplemented with 5% FBS and 1× penicillin/streptomycin. PZ-HPV-7 (an immortalized normal prostate epithelial cell line) and DU145 cell lines were maintained in PrEGM medium (Lonza, Walkersville, MD) and RPMI1640 medium (ThermoFisher Scientific, US) supplemented with 10% FBS and 1× penicillin/streptomycin, respectively. The H2009, a non-small lung cancer, cell line was cultured in RPMI1640 medium supplemented with 5% FBS. All the cell lines were cultured at 37°C in an atmosphere of 5% CO_2 and passaged at 75% confluence.

All animal studies were performed in compliance with guidelines set by the UT Southwestern Institutional Animal Care and Use Committee. Male nu/nu nude mice (5–7 weeks of age) were purchased from Harlan (Indianapolis, IN), and male SCID mice (6–8 weeks of age) were purchased from the UT Southwestern mouse-breeding core (Wakeland Colony). To establish the PC3 tumor xenograft mouse model, PC3 cell suspension was mixed 1:1 with Matrigel (BD Biosciences, Bedford, MA) and then injected subcutaneously (2×10^6 cells per site, injection volume 100 μL) into both flanks of animals. For the H2009 tumor

model, the cell suspension was injected subcutaneously (1×10^6 cells per site, injection volume 100 μL) into the back of both shoulders of SCID mice. After injection, the animals were monitored three times a week by general observations. Small PET-CT imaging was performed when the tumors become palpable.

In vitro cell uptake and subcellular localization

To determine the uptake efficiency of CPPs, 1×10^4 cells per well were seeded in 12-well plates and allowed to grow for 24 h. Then a FITC-tagged CCP (5 μM) was added and incubated with cells for 30 min. After removal of the medium, the cells were treated with Tryphan Blue (0.4% w/v, Mediatech, Inc., Herndon, VA) to quench the extracellular fluorescence and washed three times with cold PBS. The cells were then lysed with Tris Buffer (50 mM Tris–HCl, pH 7.5, 150 mM NaCl, 5 mM EDTA, 1% Triton X-100). The fluorescence intensity was measured by SpectraMax M5 (Molecular Devices, Sunnyvale, CA) with an excitation wavelength of 490 nm, an emission wavelength of 530 nm, and a cutoff wavelength of 515 nm. The protein concentration in each well was determined using a BCA protein assay kit (Pierce, Rockford, IL). The uptake efficiency of each CPP was determined by normalizing the fluorescence intensity with the protein concentration and the relative uptake was calculated as compared to that of FITC-$NHGR_{11}$. To determine the subcellular localization of a CPP, after 30 min incubation, the cells were fixed with 4% paraformaldehyde in PBS buffer and then counterstained with 1 μg/mL DAPI (Sigma, St. Louis, MO). Each sample was examined under a fluorescence microscope.

Preparation of ^{64}Cu-DOTA-$NHGR_{11}$

To a 1.5 mL vial containing 10 μg DOTA-$NHGR_{11}$ in 200 μL of 0.4 M NH_4OAc solution (pH 6.5), 2–3 mCi of ^{64}Cu in 0.1 M HCl was added. The reaction mixture was vortexed and then incubated at 37°C. After 30-min incubation, 5 μL of 5 mM diethylenetriaminepentaacetic acid (DTPA) was added and the reaction mixture was incubated at room temperature for 5 min. The separation of ^{64}Cu-DOTA-$NHGR_{11}$ from ^{64}Cu-DTPA was carried out by passing the reaction mixture through a light C-18 Sep-Pak cartridge. After three times of washings with PBS, the product was eluted with 80% ethanol solution. Radio-TLC analysis was performed on a Rita Star Radioisotope TLC Analyzer (Straubenhardt, Germany) to monitor the radiolabeling reaction using ITLC paper as the plate and 10 mM PBS as the mobile phase. High performance liquid chromatography (HPLC) analysis was conducted to determine the radiochemical purity of the products using a Waters 600 Multisolvent Delivery System equipped with a Waters 2996 Photodiode Array (PDA) detector and an in-line Shell Jr. 2000 radio-detector (Fredericksburg, VA) on a Waters Xterra column (150 × 4.6 mm, 5 μm). The mobile phase was H_2O with 0.1% TFA (solvent A) and acetonitrile with 0.1% TFA (solvent B). The gradient was 5–20% B in 0–5 min and 20–40% B in 5–25 min at 1.0 mL/min flow rate.

The cold reference of ^{nat}Cu-DOTA-$NHGR_{11}$ was prepared by reacting 1 mg (0.46 μmol) of DOTA-$NHGR_{11}$ with 62 μg (0.46 μmol) of $CuCl_2$ in 1 mL of 0.4 M NH_4OAc solution at 37°C for 1 h. The product was purified by HPLC using the same condition described above and characterized by MALDI-Mass (MALDI-TOF/MS: 2242.1 [$M + H^+$]). The fraction corresponding to ^{nat}Cu-DOTA-$NHGR_{11}$ was lyophilized and stored for use as cold standard.

Biodistribution and pharmacokinetic studies

The biodistribution studies were performed in control and PC3 tumor-bearing male nu/nu nude mice. Each mouse was injected intraperitoneally with a FITC-tagged CPP at a dose of 5 nmol/g of body weight. The animals were killed at 24 h post-injection (p.i.) and the organs of interest [prostate, seminal vesicle (SV), coagulation gland (CG), testis, liver, spleen, kidneys, muscle, lung, brain, and tumor] were excised, weighed, and measured by the fluorescence reader. The relative FITC intensity of each CPP was calculated as fluorescence intensity per gram of tissue weight.

Pharmacokinetic parameters were estimated by a two-compartment model using normal male nu/nu nude mice. Blood (~5 μL) was drawn from the retro-orbital sinus of the mice at 5, 10, 20, and 40 min after the tail vein injection of ^{64}Cu-DOTA-$NHGR_{11}$, and then counted on a γ-counter.

Small animal PET/CT imaging

When the tumor size reached the range of 50–300 mm^3, the tumor-bearing mice were randomized for the PET-CT imaging with ^{64}Cu-DOTA-$NHGR_{11}$. The injected dose was 3.7 MBq of ^{64}Cu-activity in 100 μL of PBS, while the injected molar amount of NH_2GR_{11} was maintained at the same level by decay correction.

Ten minutes prior to imaging, the animal was anesthetized using 3% isofluorane at room temperature until stable vitals were established. Once the animal was sedated, it was placed onto the imaging bed under 2% isofluorane anesthesia for the duration of the imaging. The CT imaging was acquired at 80 kV and 500 μA with a focal spot of 58 μm. The total rotation of the gantry was 360° with 360 rotation steps obtained at an exposure time of approximately 235 ms/frame. The images were attained using a CCD readout of 4,096 × 3,098 with a bin factor of 4 and

an average frame of 1. Under low magnification, the effective pixel size was 103.03 μm. Total CT scan time was approximately 6 min. CT images were reconstructed with a down sample factor of 2 using Cobra Reconstruction Software. The PET imaging was performed directly after the acquisition of CT data. The PET tracer was injected intravenously via the tail vein. Static PET scans were performed at 1, 4, and 24 h p.i. for 15 min. PET images at 1, 4, and 24 h p.i. were reconstructed using Fourier Rebinning and Ordered Subsets Expectation Maximization 3D (OSEM3D) algorithm. Reconstructed CT and PET images were fused and analyzed using the Siemens Inveon Research Workplace (IRW) software. For quantification, regions of interest were placed in the areas expressing the highest radiotracer activity as determined by visual inspection. The tissues examined include the left and right tumors, heart, liver, lung, kidneys, and muscle. The resulting quantitative data were expressed as percent injected dose per gram of tissue (%ID/g).

Statistical analysis

Quantitative data were expressed as mean ± SD and then compared using one-way analysis of variance and Student's *t* test. *P* values <0.05 were considered statistically significant.

Results

In vitro cell uptake and subcellular localization

The oligoarginine length effect on the cell uptake efficiency was evaluated using FITC-$NHGR_9$, FITC-$NHGR_{11}$ and FITC-$NHGR_{13}$ in four different human prostate cell lines: PZ-HPV-7, LNCaP, PC3, and DU145. For comparison, the uptake of FITC-$NHGR_{11}$ in LNCaP is set at 1.0. As shown in Fig. 1a, after 30 min incubation, FITC-$NHGR_{11}$ displayed much higher uptake efficiency

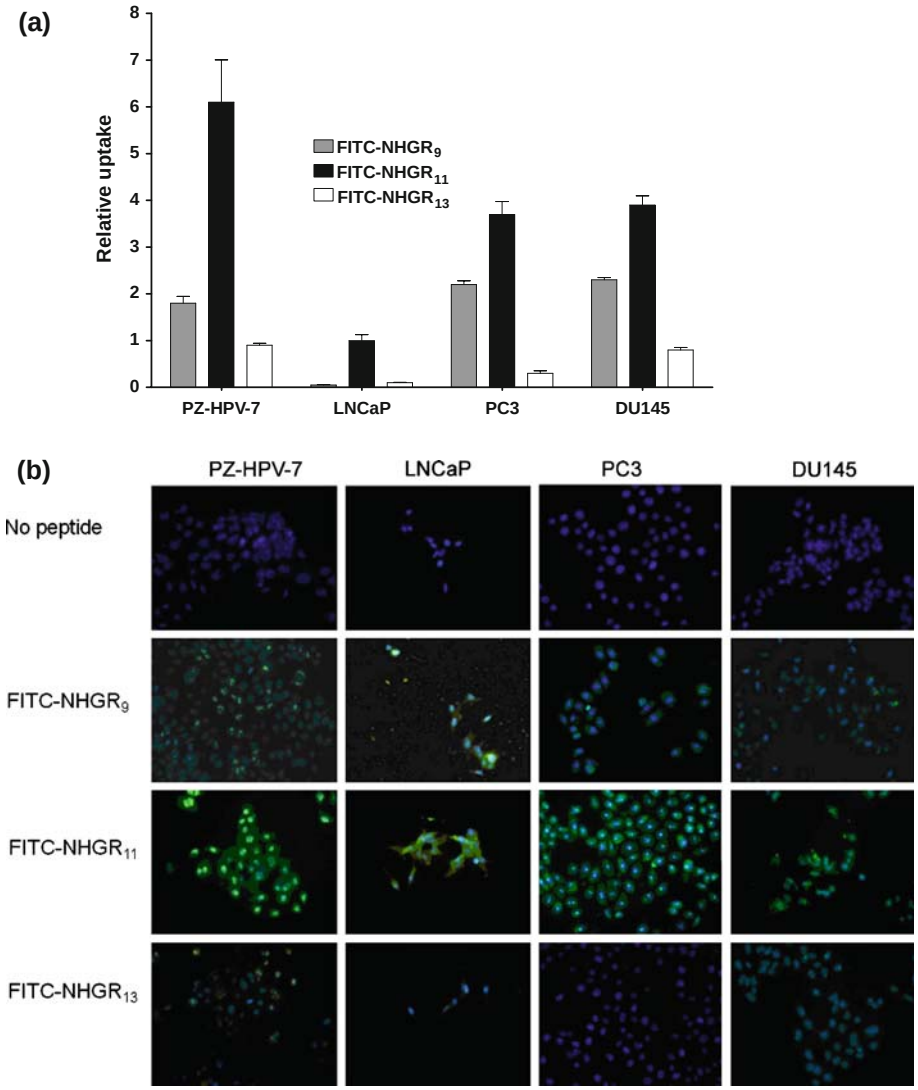

Fig. 1 Uptake of FITC-$NHGR_9$, FITC-$NHGR_{11}$, and FITC-$NHGR_{13}$ by prostate cells (PZ-HPV-7, LNCaP, PC3 and DU145). **a** FITC-$NHGR_9$, FITC-NH_2GR_{11}, and FITC-NH_2GR_{13} were incubated with cells for 30 min before cell harvesting. Relative FITC intensity was determined by normalizing fluorescence intensity with its protein content and presented as relative level compared to uptake of FITC-$NHGR_{11}$ in LNCaP. *Columns* mean in triplicate, *bars* SD. All the experiments were repeated at least twice. **b** Cells were incubated with 5 μmol/L of the indicated peptide for 30 min. After fixation, cells were counterstained with DAPI. The cellular distribution of each peptide was visualized with a fluorescence microscope

than FITC-$NHGR_9$ and FITC-$NHGR_{13}$ ($P < 0.005$) in all the four cell lines indicating that the intracellular uptake of oligoarginines is greatly affected by the number of the repeating guanidino moiety. Of the three FITC-tagged oligoarginines, FITC-$NHGR_{13}$ showed the lowest uptake in three of the tested cell lines (PZ-HPV-7, PC3, and DU145). In PC3 and DU145, FITC-$NHGR_9$ displayed appreciable uptake values, which are 63 and 65% of that of FITC-$NHGR_{11}$, respectively. Overall, the PZ-HPV-7 and LNCaP cell lines exhibited highly selective internalization of oligoarginines varying with the peptide length.

The subcellular localization of FITC-$NHGR_9$, FITC-$NHGR_{11}$, and FITC-$NHGR_{13}$ in the prostate cancer cell lines was shown in Fig. 1b. Apparently, FITC-$NHGR_{11}$ exhibited a higher fluorescent intensity in all the cell lines. The majority of FITC-$NHGR_{11}$ was localized in the cytosol, while in PZ-HPV-7 and PC3 cell lines, nuclear staining with FITC-$NHGR_{11}$ was also seen. Both FITC-$NHGR_9$ and FITC-$NHGR_{13}$ showed significantly lower fluorescent intensity than FITC-$NHGR_{11}$ in all four tested cell lines, which is consistent with the cell uptake results. Taken together, these data demonstrate the high efficiency and amino acid length-dependent uptake of FITC-$NHGR_{11}$ in various prostate cell lines, which has made FITC-$NHGR_{11}$ as a unique probe for detecting prostate cancer.

Preparation of ^{64}Cu-DOTA-$NHGR_{11}$

To label NH_2GR_{11} with ^{64}Cu, a commonly used bifunctional chelator, DOTA was conjugated to the N terminus of the peptide. The conjugate, DOTA-$NHGR_{11}$, was labeled with ^{64}Cu by incubating with $^{64}Cu^{2+}$ in 0.4 M NH_4OAc buffer (pH 6.5) at 37°C for 30 min. Non-specifically bound ^{64}Cu was removed in the form of ^{64}Cu-DTPA at the end of the radiolabling procedure. The radiolabeling reaction was monitored by radio-TLC analysis, in which the reaction mixture was sampled on an instant TLC plate that was then developed in PBS buffer. Under the TLC conditions, ^{64}Cu-DOTA-$NHGR_{11}$ stayed at the origin, while ^{64}Cu-DTPA moved to the solvent front. The radiochemical yield was >90% when 10 μg of the DOTA conjugate was used to label 2–3 mCi of ^{64}Cu. The ^{64}Cu-DTPA was removed by passing the reaction mixture through a light C18 Sep-Pak cartridge and three times of washing with PBS. The product, ^{64}Cu-DOTA-$NHGR_{11}$, could then be efficiently eluted with 80% of ethanol. The radiochemical purity of ^{64}Cu-DOTA-$NHGR_{11}$ was nearly 100% after the Sep-Pak purification as determined by radio-ITLC and radio-HPLC.

To confirm the identity of the labeled product, ^{nat}Cu-DOTA-$NHGR_{11}$ was prepared and used as a reference standard. Both ^{64}Cu-DOTA-$NHGR_{11}$ and ^{nat}Cu-DOTA-$NHGR_{11}$ showed a single peak on HPLC (^{64}Cu-DOTA-$NHGR_{11}$: radioactivity detector; ^{nat}Cu-DOTA-$NHGR_{11}$: PDA UV detector) with the same retention time within 14–15 min.

Biodistribution and in vivo pharmacokinetics

The tissue distribution of FITC-$NHGR_9$, FITC-$NHGR_{11}$, and FITC-$NHGR_{13}$ was conducted in control and PC-3 tumor-bearing nude mice. The biodistribution data are presented in Figs. 2 and 3, respectively. For comparison, the uptake value of FITC-$NHGR_9$ in the prostate is set at 1.0 in Fig. 2. Compared to FITC-$NHGR_9$ and FITC-$NHGR_{13}$, FITC-$NHGR_{11}$ clearly showed preferential accumulation in the prostate tissue as measured by the uptake ratios of the prostate to other organs. As shown in Fig. 3, FITC-$NHGR_{11}$ displayed high relative uptake values in both prostate tissue and prostate tumor. Impressively, the uptake ratios of tumor to muscle and prostate to muscle were 3.8 and 8.7, respectively. In addition, FITC-$NHGR_{11}$ showed low uptake in the major clearance organs (e.g. liver, spleen, and kidneys).

Given the limited capability of fluorescence imaging quantification for in vivo evaluations, the in vivo pharmacokinetics of NH_2GR_{11} was evaluated using ^{64}Cu-DOTA-$NHGR_{11}$ in normal mice based on a two-compartment model. Its half-life in the blood (the primary compartment) was 10.7 min; and the elimination half-life from other organs (the secondary compartment) was 17.2 h.

Small animal PET-CT imaging

The comparative small animal imaging evaluation of ^{64}Cu-DOTA-$NHGR_{11}$ was performed using PC3 and H2009 tumor-bearing SCID mice, which were injected with a

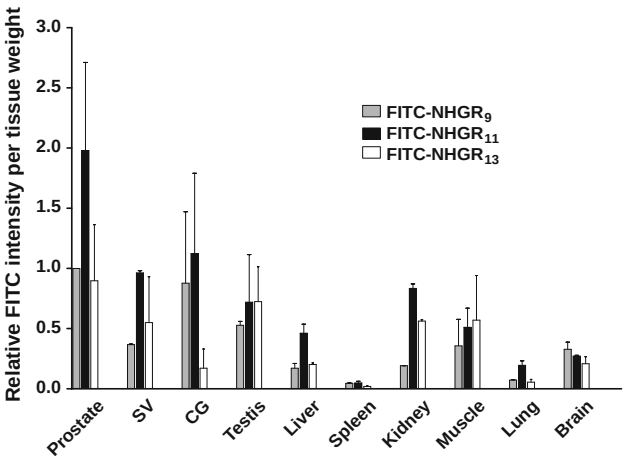

Fig. 2 Biodistribution of FITC-$NHGR_9$, FITC-$NHGR_{11}$, and FITC-$NHGR_{13}$ in normal male nu/nu nude mice at 24 h p.i. ($n = 3$). *SV* seminal vesicle and *CG* coagulation gland

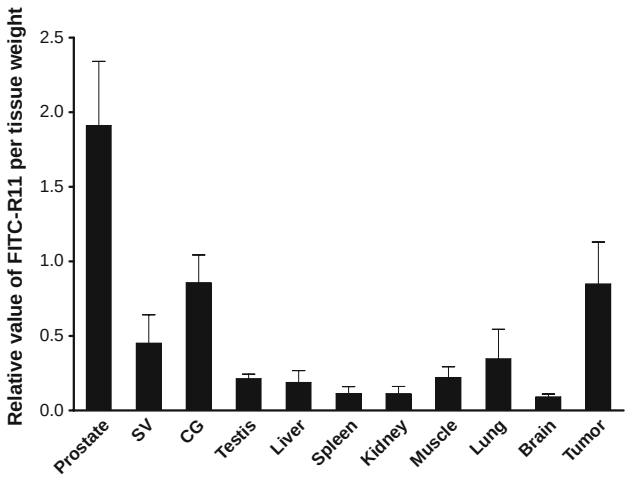

Fig. 3 Biodistribution of FITC-$NHGR_{11}$ in PC3 tumor-bearing mice at 24 h p.i. ($n = 4$)

similar amount of peptide with respect to the volume of tumor as calculated based on the specificity radioactivity of ^{64}Cu-DOTA-$NHGR_{11}$. The PET-CT imaging acquisition was conducted at 1, 4, and 24 h p.i. ($n = 3$ at each time point). The representative PET-CT images (transaxial) are presented in Fig. 4. Clearly the PC3 tumors on both flanks were visualized by ^{64}Cu-DOTA-$NHGR_{11}$ on PET images at 1, 4 and 24 h p.i. In contrast, the H2009 tumors were only visible at 1 and 4 h with much lower signal intensity on PET as compared to the PC3 tumors; at 24 h p.i., they became not detectable.

The PET images were quantitatively analyzed by the Siemens Inveon Research Workplace (IRW) software. Summarized in Table 1 are the uptake values of ^{64}Cu-DOTA-$NHGR_{11}$ in the regions of interest [tumors (left and right), heart, liver, lung, kidney (left), and muscle] obtained from the imaging quantification. Not surprisingly, ^{64}Cu-DOTA-$NHGR_{11}$ showed nearly identical uptake values in the right and left tumors. The accumulation level of ^{64}Cu-DOTA-$NHGR_{11}$ in the PC3 tumors remained steady out to 24 h p.i. (1.17 ± 0.19%ID/g at 1 h p.i.; 0.91 ± 0.32%ID/g at 4 h; 24 h 0.82 ± 0.24%ID/g at 24 h), whereas its uptake in the H2009 tumors was significantly lower ($P < 0.02$) and showed an appreciable trend of decreases over time (0.81 ± 0.07%ID/g at 1 h p.i.; 0.47 ± 0.12%ID/g at 4 h; 24 h 0.33 ± 0.05%ID/g at 24 h). Impressively, the uptake ratios of ^{64}Cu-DOTA-$NHGR_{11}$ in PC3 tumor versus muscle at 1, 4, and 24 h p.i. were 5.06 ± 0.96, 4.87 ± 1.29, and 10.41 ± 6.07, respectively. In other organs, ^{64}Cu-DOTA-$NHGR_{11}$ exhibited a very similar distribution pattern in both tumor-bearing mouse models.

Discussion

In spite of the extensive utilization of arginine-rich CPPs for intracellular delivery of a broad range of bioactive materials, the internalization mechanisms of CPPs are still under investigation. It has been reported that a slight structural alteration might lead to significant changes of the CPP internalization mechanisms or subcellular localization, which can thereby considerably affect its internalization efficiency and the bioavailability of its cargos (Nakase et al. 2008). Internalization selectivity of CPPs into specific cells or organs is highly desirable for efficient target delivery of therapeutics in order to minimize the side effects on non-target organs. This selectivity can be obviously imparted by attaching a targeting molecule to the CPP-cargo conjugate, although it adds complexity to the overall construct. From screening of various CPPs for the potential candidate of delivery vehicle in prostate cancer, we have reported that an arginine-rich CPP exhibits a high efficiency of intracellular uptake in vitro (Zhou et al. 2006). In 2007, Elson-Schwab et al. (2007) reported that the delivery of arginine-rich CPPs at nanomolar transporter concentrations was completely mediated by the membrane-associated heparan sulfate proteoglycans (HSPG). Given the fact that the expression level of HSPG varies with cell type (Sasisekharan et al. 2002; Sanderson et al. 2004), it is not surprising that CPPs with certain structure or sequence may display cell or organ specificity to some extent. Indeed, the fact that the negatively charged heparan

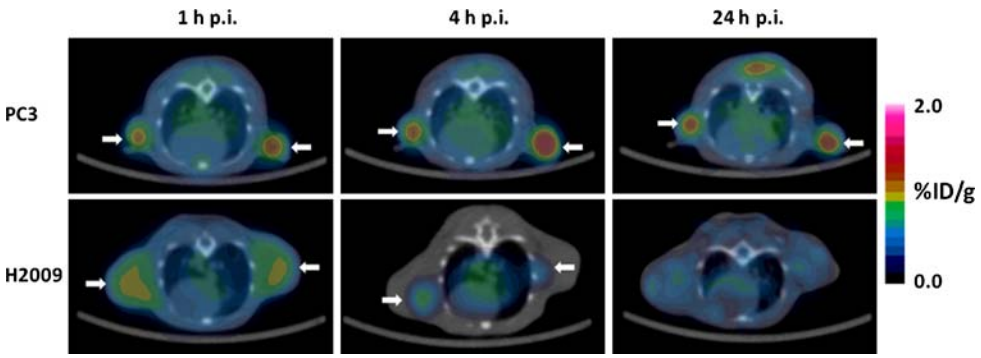

Fig. 4 Representative transaxial PET-CT images of ^{64}Cu-DOTA-$NHGR_{11}$ in PC3 and H2009 tumor-bearing mice at 1, 4, and 24 h p.i. ($n = 3$). The *white arrows* indicate tumors

Table 1 PET quantification data of ^{64}Cu-DOTA-NHGR$_{11}$ in PC3 and H2009 tumor-bearing mice at 1, 4, and 24 h p.i.

%ID/g	PC3 tumor model			H2009 tumor model		
	1 h	4 h	24 h	1 h	4 h	24 h
Tumor	1.17 ± 0.19**	0.91 ± 0.32*	0.82 ± 0.24***	0.81 ± 0.07**	0.47 ± 0.12*	0.33 ± 0.05***
Heart	0.58 ± 0.06	0.52 ± 0.03	0.40 ± 0.06	0.72 ± 0.05	0.43 ± 0.13	0.39 ± 0.03
Liver	9.13 ± 1.75	7.95 ± 1.91	5.03 ± 1.17	8.13 ± 0.12	7.63 ± 0.31	7.20 ± 0.46
Lung	0.59 ± 0.07	0.62 ± 0.10	0.43 ± 0.08	0.55 ± 0.04	0.27 ± 0.05	0.31 ± 0.09
Kidneys	3.93 ± 0.21	3.40 ± 0.00	1.73 ± 0.06	4.27 ± 0.15	4.33 ± 0.35	2.10 ± 0.26
Muscle	0.24 ± 0.06	0.18 ± 0.03	0.09 ± 0.05	0.24 ± 0.03	0.15 ± 0.09	0.09 ± 0.01

Data are presented as %ID/g ± SD ($n = 3$; *$P < 0.02$; **$P < 0.002$; ***$P < 0.001$)

sulfates on HSPG can form divalent hydrogen-bonds with the guanidino groups (Nakase et al. 2008) may explain the role of HSPG in the internalization of arginine-rich CPPs.

Heparan sulfate proteoglycans consist of a diverse family of glycosaminoglycan-bearing protein cores including the syndecans and perlecan (Kirn-Safran et al. 2009). Recently, Datta et al. (2006) reported that perlecan, also called HSPG-2, is highly expressed in various prostate cancer cell lines including LNCaP, PC3, and DU145, and the cell growth is inhibited by silencing the expression of perlecan. In addition, the level of perlecan in prostate cancer tissues was found in good correlation with the Gleason score and rapid cell proliferation. Similarly, syndecan-1, a cell membrane-bound HSPG, was reported with a great overexpression during the androgen-independent progression of prostate cancer in a mouse model (Alexander et al. 2000) and the androgen-independent prostate cancer cell lines, such as PC3 and DU145 (Chen et al. 2004a, b).

The preferential uptake of NH_2GR_{11} that we observed in various prostate cancer cell lines could be reasonably explained by the upregulated expression of HSPG in prostate tissues or cancer cells. This prompted us to speculate the potential application of NH_2GR_{11} as PET imaging probe for the diagnosis of prostate cancer, while the detailed mechanism of this specific uptake may take years of research to reveal. It is noteworthy that other CPPs with different sequences or lengths may exhibit similar or even better prostate tissue uptake specificity. Given the high uptake of NH_2GR_{11} was also observed in the normal prostate tissue (Figs. 2, 3), we believe that the NH_2GR_{11}-based PET imaging probes will be more suitable for the detection of distant prostate cancer metastases such as lymph node and bone metastases rather than primary prostate tumor. Indeed, there has been a postulation that the bone extracellular matrix is a perlecan-rich site, which explains why prostate cancer preferentially metastasizes to the bone (Datta et al. 2006).

In the present work, we first evaluated the length effect on the internalization efficiency using three FITC-tagged oligoarginines differing in the number of repeating arginine units in hope for an optimal length for the following evaluations. The in vitro cell uptake and subcellular localization experiments were performed in four different prostate cell lines. The result was what we anticipated to some extent. The CPP with 11 arginine-repeating units, NH_2GR_{11}, unequivocally demonstrated its superiority over other two CPPs with either shorter or longer length in term of absolute cell uptake and internalization efficiency (Fig. 1). As shown in Fig. 1b, NH_2GR_{11} was primarily presented in the cytosol after being internalized.

Given the in vitro result, we proceeded to evaluate whether NH_2GR_{11} could maintain the superior properties in normal nude mice as compared to NH_2GR_9 and NH_2GR_{13}. As measured by the uptake ratios of the prostate to other organs, a clear preferential accumulation in the prostate tissue was observed for FITC-NHGR$_{11}$ but not for either FITC-NHGR$_9$ or FITC-NHGR$_{13}$. This overall in vivo uptake result of the three FITC-tagged peptides is similar to the in vitro result, indicating that the biologic activity of these CPPs remains quite consistent under the environment of different tissue types. Nevertheless, this high uptake in normal prostate tissue exhibited by FITC-NHGR$_{11}$ precludes NH_2GR_{11} from being considered as imaging probes for primary prostate cancer detection. However, it can be well suited for the detection of distant prostate cancer metastases. As such we further evaluated the biodistribution profile of FITC-NHGR$_{11}$ in PC3 tumor-bearing animal with the tumor distant from the normal prostate (Fig. 3). In addition to the expected high uptake in the prostate, FITC-NHGR$_{11}$ showed elevated accumulation in the PC3 tumor, which serves as an analogic model of distant prostate cancer metastasis.

The in vivo pharmacokinetics of NH_2GR_{11} evaluated with ^{64}Cu-DOTA-NHGR$_{11}$ in normal mice showed that the CPP was cleared from the blood rapidly with a half-life of 10.7 min, but its elimination half-life from other organs

(the secondary compartment) was rather long (17.2 h). This was why we chose ^{64}Cu ($t_{1/2}$: 12.7 h) instead of ^{18}F ($t_{1/2}$: 110 min) for the PET application of NH_2GR_{11}.

The labeling of DOTA-$NHGR_{11}$ with ^{64}Cu was straightforward. The radiochemical yields were reasonably high. After the purification by a light C18 Sep-Pak cartridge, the radiochemical purity of ^{64}Cu-DOTA-$NHGR_{11}$ was nearly 100% as determined by a reverse phase HPLC method. The specific radioactivity of ^{64}Cu-DOTA-$NHGR_{11}$ was 11 GBq/μmol.

With the goal to develop NH_2GR_{11} for specific PET imaging of prostate cancer metastases, we designed and performed a comparative PET-CT imaging experiment using PC3 and H2009 tumor-bearing mouse models. However, due to the availability of ^{64}Cu and the tumor-growth rate difference between PC3 and H2009, the tumor sizes of PC3 and H2009 could not be ideally matched for this preliminary evaluation. The PC3 tumors were around 100 mm^3 at the time of PET-CT imaging, while the H2009 tumor size was in the range of 100–300 mm^3. However, the PC3 tumors were clearly visualized with ^{64}Cu-DOTA-$NHGR_{11}$ at 1, 4, and 24 h p.i., while the H2009 tumors became invisible on PET images after 4 h p.i. The PET imaging quantification further confirmed that the absolute uptake of ^{64}Cu-DOTA-$NHGR_{11}$ in the PC3 tumors was significantly higher than in the H2009 tumors throughout the imaging study, indicating the desired imaging specificity of ^{64}Cu-DOTA-$NHGR_{11}$. The slow clearance of ^{64}Cu-DOTA-$NHGR_{11}$ from the PC3 tumors likely reflects the fact that the radiotracer had been internalized into the tumor cells within 1 h p.i., while the significant clearance of ^{64}Cu-DOTA-$NHGR_{11}$ from the H2009 tumors probably indicates that the radiotracer could not be efficiently internalized into the lung cancer cells. Intriguingly, there are reports that the syndecan-1 expression is lost in lung cancer (Nackaerts et al. 1997; Chen et al. 2004a, b).

It is noteworthy that the biodistribution profiles of NH_2GR_{11} obtained from FITC-$NHGR_{11}$ and ^{64}Cu-DOTA-$NHGR_{11}$ (Fig. 2; Table 1) are not in good agreement with regard to the uptake values in the liver and kidneys. While the discrepancies might be caused by the different administration routes of FITC-$NHGR_{11}$ and ^{64}Cu-DOTA-$NHGR_{11}$, the high accumulation of ^{64}Cu-DOTA-$NHGR_{11}$ in the liver could be partially resulted from the dislocation of ^{64}Cu from the DOTA moiety (Boswell et al. 2004). To circumvent this in vivo stability problem, in our future evaluations of NH_2GR_{11}, we will replace the DOTA moiety with a cross-bridged tetraazamacrocyclic bifunctional chelator (CB-TE2A: 4,11-bis(carboxymethyl)-1,4,8,11-tetraazabicyclo[6.6.2]hexadecane) whose ^{64}Cu-complex has been shown with strong resistance to the in vivo transchelation of ^{64}Cu (Sun et al. 2002).

Conclusions

We have demonstrated the potential of using $NHGR_{11}$ to develop specific PET imaging probes for distant prostate cancer metastases by both in vitro and in vivo evaluations performed with FITC-$NHGR_{11}$ and ^{64}Cu-DOTA-$NHGR_{11}$. Further mechanistic elucidation of the cell uptake and internalization of arginine-rich CPPs would facilitate the development of this unique group of molecules for targeted molecular imaging and drug delivery.

Acknowledgments This work was partially supported by the Prostate Cancer Research Program of the United States Army Medical Research and Materiel Command (W81XWH-08-1-0305 and W81XWH-04-1-0222), a Clinical Innovator Award from the Flight Attendant Medical Research Institute, and a small animal imaging research program grant (SAIRP) from the National Institute of Cancer (U24 CA126608). The authors acknowledge the generous support of a private donor that allowed the purchase of the Siemens Inveon PET-CT Multi-modality System.

References

Albrecht S, Buchegger F, Soloviev D, Zaidi H, Vees H, Khan HG, Keller A, Bischof Delaloye A, Ratib O, Miralbell R (2007) (11)C-acetate PET in the early evaluation of prostate cancer recurrence. Eur J Nucl Med Mol Imaging 34(2):185–196

Alexander CM, Reichsman F, Hinkes MT, Lincecum J, Becker KA, Cumberledge S, Bernfield M (2000) Syndecan-1 is required for Wnt-1-induced mammary tumorigenesis in mice. Nat Genet 25(3):329–332

Beheshti M, Langsteger W, Fogelman I (2009) Prostate cancer: role of SPECT and PET in imaging bone metastases. Semin Nucl Med 39(6):396–407

Boswell CA, Sun XK, Niu WJ, Weisman GR, Wong EH, Rheingold AL, Anderson CJ (2004) Comparative in vivo stability of copper-64-labeled cross-bridged and conventional tetraazamacrocyclic complexes. J Med Chem 47(6):1465–1474

Bouchelouche K, Capala J, Oehr P (2009) Positron emission tomography/computed tomography and radioimmunotherapy of prostate cancer. Curr Opin Oncol 21(5):469–474

Bucci M, Gratton JP, Rudic RD, Acevedo L, Roviezzo F, Cirino G, Sessa WC (2000) In vivo delivery of the caveolin-1 scaffolding domain inhibits nitric oxide synthesis and reduces inflammation. Nat Med 6(12):1362–1367

Chen D, Adenekan B, Chen L, Vaughan ED, Gerald W, Feng Z, Knudsen BS (2004a) Syndecan-1 expression in locally invasive and metastatic prostate cancer. Urology 63(2):402–407

Chen XY, Park R, Hou YP, Tohme M, Shahinian AH, Bading JR, Conti PS (2004b) MicroPET and autoradiographic imaging of GRP receptor expression with Cu-64-DOTA-[Lys(3)]bombesin in human prostate adenocarcinoma xenografts. J Nucl Med 45(8):1390–1397

Datta MW, Hernandez AM, Schlicht MJ, Kahler AJ, DeGueme AM, Dhir R, Shah RB, Farach-Carson C, Barrett A, Datta S (2006) Perlecan, a candidate gene for the CAPB locus, regulates prostate cancer cell growth via the Sonic Hedgehog pathway. Mol Cancer 5:9

Elson-Schwab L, Garner OB, Schuksz M, Crawford BE, Esko JD, Tor Y (2007) Guanidinylated neomycin delivers large, bioactive

cargo into cells through a heparan sulfate-dependent pathway. J Biol Chem 282(18):13585–13591

Emonds KM, Swinnen JV, Mortelmans L, Mottaghy FM (2009) Molecular imaging of prostate cancer. Methods 48(2):193–199

Etchebehere ECSC, Macapinlac HA, Gonen M, Humm J, Yeung HWD, Akhurst T, Scher HI, Larson SM (2002) Qualitative and quantitative comparison between images obtained with filtered back projection and iterative reconstruction in prostate cancer lesions on F-18-FDG PET. Q J Nucl Med 46(2):122–130

Fogelman I, Cook G, Israel O, Van der Wall H (2005) Positron emission tomography and bone metastases. Semin Nucl Med 35(2):135–142

Gambhir SS (2002) Molecular imaging of cancer with positron emission tomography. Nat Rev Cancer 2(9):683–693

Giovacchini G, Gajate AM, Messa C, Fazio F (2008) Increased C-11 choline uptake in pagetic bone in a patient with coexisting skeletal metastases from prostate cancer. Clin Nucl Med 33(11):797–798

Gratton JP, Yu J, Griffith JW, Babbitt RW, Scotland RS, Hickey R, Giordano FJ, Sessa WC (2003) Cell-permeable peptides improve cellular uptake and therapeutic gene delivery of replication-deficient viruses in cells and in vivo. Nat Med 9(3):357–362

Hara T, Kosaka N, Kishi H (1998) PET imaging of prostate cancer using carbon-11-choline. J Nucl Med 39(6):990–995

Kirn-Safran C, Farach-Carson MC, Carson DD (2009) Multifunctionality of extracellular and cell surface heparan sulfate proteoglycans. Cell Mol Life Sci 66(21):3421–3434

Langsteger W, Heinisch M, Fogelman I (2006) The role of fluorodeoxyglucose, 18F-dihydroxyphenylalanine, 18F-choline, and 18F-fluoride in bone imaging with emphasis on prostate and breast. Semin Nucl Med 36(1):73–92

Larson SM, Morris M, Gunther I, Beattie B, Humm JL, Akhurst TA, Finn RD, Erdi Y, Pentlow K, Dyke J, Squire O, Bornmann W, McCarthy T, Welch M, Scher H (2004) Tumor localization of 16beta-18F-fluoro-5alpha-dihydrotestosterone versus 18F-FDG in patients with progressive, metastatic prostate cancer. J Nucl Med 45(3):366–373

Maeda T, Tateishi U, Komiyama M, Fujimoto H, Watanabe S, Terauchi T, Moriyama N, Arai Y, Sugimura K, Kakizoe T (2006) Distant metastasis of prostate cancer: early detection of recurrent tumor with dual-phase carbon-11 choline positron emission tomography/computed tomography in two cases. Jpn J Clin Oncol 36(9):598–601

Nackaerts K, Verbeken E, Deneffe G, Vanderschueren B, Demedts M, David G (1997) Heparan sulfate proteoglycan expression in human lung-cancer cells. Int J Cancer 74(3):335–345

Nakase I, Takeuchi T, Tanaka G, Futaki S (2008) Methodological and cellular aspects that govern the internalization mechanisms of arginine-rich cell-penetrating peptides. Adv Drug Deliver Rev 60(4–5):598–607

Oyama N, Miller TR, Dehdashti F, Kibel AS, Michalski JM, Fischer KC, Picus J, Siegel BA, Andriole GL, Welch MJ (2002) Carbon-11-acetate PET imaging of recurrent prostate cancer. J Urol 167(4):173–174

Oyama N, Ponde DE, Dence C, Kim J, Tai YC, Welch MJ (2004) Monitoring of therapy in androgen-dependent prostate tumor model by measuring tumor proliferation. J Nucl Med 45(3):519–525

Ponde DE, Dence CS, Oyama N, Kim J, Tai YC, Laforest R, Siegel BA, Welch MJ (2007) 18F-fluoroacetate: a potential acetate analog for prostate tumor imaging—in vivo evaluation of 18F-fluoroacetate versus 11C-acetate. J Nucl Med 48(3):420–428

Rogers BE, Bigott HM, McCarthy DW, Della Manna D, Kim J, Sharp TL, Welch MJ (2003) MicroPET imaging of a gastrin-releasing peptide receptor-positive tumor in a mouse model of human prostate cancer using a 64Cu-labeled bombesin analogue. Bioconjug Chem 14(4):756–763

Rothbard JB, Jessop TC, Lewis RS, Murray BA, Wender PA (2004) Role of membrane potential and hydrogen bonding in the mechanism of translocation of guanidinium-rich peptides into cells. J Am Chem Soc 126(31):9506–9507

Sakai N, Takeuchi T, Futaki S, Matile S (2005) Direct observation of anion-mediated translocation of fluorescent oligoarginine carriers into and across bulk liquid and anionic bilayer membranes. ChemBioChem 6(1):114–122

Sanderson RD, Yang Y, Suva LJ, Kelly T (2004) Heparan sulfate proteoglycans and heparanase-partners in osteolytic tumor growth and metastasis. Matrix Biol 23(6):341–352

Sasisekharan R, Shriver Z, Venkataraman G, Narayanasami U (2002) Roles of heparan-sulphate glycosaminoglycans in cancer. Nat Rev Cancer 2(7):521–528

Schuhmacher J, Zhang H, Doll J, Macke HR, Matys R, Hauser H, Henze M, Haberkorn U, Eisenhut M (2005) GRP receptor-targeted PET of a rat pancreas carcinoma xenograft in nude mice with a 68 Ga-labeled bombesin(6–14) analog. J Nucl Med 46(4):691–699

Shreve PD, Grossman HB, Gross MD, Wahl RL (1996) Metastatic prostate cancer: initial findings of PET with 2-deoxy-2-[F-18]fluoro-D-glucose. Radiology 199(3):751–756

Sun XK, Wuest M, Weisman GR, Wong EH, Reed DP, Boswell CA, Motekaitis R, Martell AE, Welch MJ, Anderson CJ (2002) Radiolabeling and in vivo behavior of copper-64-labeled cross-bridged cyclam ligands. J Med Chem 45(2):469–477

Vees H, Buchegger F, Albrecht S, Khan H, Husarik D, Zaidi H, Soloviev D, Hany TF, Miralbell R (2007) F-18-choline and/or C-11-acetate positron emission tomography: detection of residual or progressive subclinical disease at very low prostate-specific antigen values (<1 ng/mL) after radical prostatectomy. BJU Int 99(6):1415–1420

Yang YS, Zhang XZ, Xiong ZM, Chen XY (2006) Comparative in vitro and in vivo evaluation of two Cu-64-labeled bombesin analogs in a mouse model of human prostate adenocarcinoma. Nucl Med Biol 33(3):371–380

Zhang X, Cai W, Cao F, Schreibmann E, Wu Y, Wu JC, Xing L, Chen X (2006) 18F-labeled bombesin analogs for targeting GRP receptor-expressing prostate cancer. J Nucl Med 47(3):492–501

Zhou J, Fan J, Hsieh JT (2006) Inhibition of mitogen-elicited signal transduction and growth in prostate cancer with a small peptide derived from the functional domain of DOC-2/DAB2 delivered by a unique vehicle. Cancer Res 66(18):8954–8958